Measuring Significant Wave Height fields in two dimensions at kilometric scales with SWOT.

Alejandro Bohé, Albert Chen, Curtis Chen, Pierre Dubois, Alexander Fore, Beatriz Molero, Eva Peral, Matthias Raynal, Bryan Stiles, Fabrice Ardhuin, Andrea Hay, Benoît Legresy, Luc Lenain and Ana B. Villas Bôas

***Abstract*—We demonstrate that spatial maps of Significant Wave Height (SWH) with kilometric resolutions can be derived from the data acquired by the KaRIn instrument on-board the SWOT mission by exploiting the measured interferometric decorrelation. We discuss the sensitivity to errors in the volumetric decorrelation estimates and show that a succesful inversion of SWH, particularly in the outer part of KaRIn's swath and for low values of SWH, requires factoring out all sources of decorrelation of instrumental origin to an exquisite precision. We then validate KaRIn's SWH measurement against independent data, namely GPS buoys, airborne lidar, Sentinel3, SWOT's nadir altimeter and the ECMWF global wave model. We show that biases between KaRIn and the other sensors are centimetric and that KaRIn is able to capture features in the two dimensional SWH field of only a few kilometers. While KaRIn's SWH measurement error is difficult to fully characterize due the absence of two-dimensional ground truth data valid at such fine spatial scales and spanning a wide range of sea states, we argue that the retrieved fields are dominated by signal rather than noise, except possibly in the last few kilometers of the swath at low SWH. We briefly discuss the implications in terms of advancing our understanding of the phenomena that shape the wave fields at small scales. The algorithm and calibration described in this paper will be the basis for version D of the operational SWOT products.**

***Index Terms*—Significant Wave Height (SWH), Surface Water Ocean Topography (SWOT), Ka-Band Radar Interferometer (KaRIn)**

I. Introduction

The Surface Water and Ocean Topography (SWOT) mission [1]–[3] is primarily designed to measure Sea Surface Height (SSH) in two dimensions at an unprecedented resolution (see for instance [4]) thanks to its innovative Ka-band radar interferometer KaRIn. In addition to the topography measurements derived from the phase difference between the images acquired at each of the two antennas separated by approximately 10 meters, KaRIn can also provide information about sea state, by exploiting the measured power in each of the SAR images and the interferometric correlation between both acquisition channels. This last quantity, sometimes referred to as interferometric coherence, is directly affected by the presence of surface waves. This in turn provides an opportunity to measure, for the first time at a global scale, significant wave height at kilometric resolutions (well below the reach of nadir altimeters) and in two dimensions. This, however, requires estimating all other sources of decorrelation of instrumental origin with an exquisite precision to avoid misinterpreting instrumental effects as geophysical signals. In this paper, we first describe in section II how the interferometric acquisitions by KaRIn are calibrated and processed to obtain SWH spatial maps at various km-scale resolutions (typically 2x2 km, 5x5 km), and discuss how the accuracy at which we need to estimate all the other sources of decorrelation varies with cross-track distance and actual SWH to highlight the most challenging regimes for the inversion. We then present in section III comparisons between the KaRIn two-dimensional SWH measurements and several independent sets of validation data, including data from SWOT's nadir altimeter, the SAR nadir altimeter on-board Sentinel-3, MASS airborne lidar, and in-situ data. Finally, in section IV, we discuss example features observed in the retrieved SWH fields to illustrate the potential use of such high resolution two-dimensional surface wave observations from SWOT to develop better physical understanding of the processes that contribute to sea-state variations at smaller scales. We also argue here that these two-dimensional SWH measurements can be used to improve sea state bias correction.

A. Bohé and M. Raynal are with the Centre National d'Etudes Satiales, 31000 Toulouse, France.

A. Chen, C. Chen, A. Fore, E. Peral and B. Stiles are with the Jet Propulsion Laboratory (JPL), California Institute of Technology, Pasadena, CA 91011 USA.

P. Dubois and B. Molero are with Collecte Localisation Satellites, 31520 Ramonville-Saint-Agne, France.

F. Ardhuin is with the University Brest, CNRS, Ifremer, IRD, IUEM, Laboratoire d'Océanographie Physique et Spatiale (LOPS), Plouzané, France.

A. Hay is with the School of Geography, Planning, and Spatial Sciences, University of Tasmania, Hobart, Tasmania, Australia.

B. Legresy is with the Commonwealth Scientific and Industrial Research Organisation, Hobart, Tasmania, Australia.

L. Lenain is with the Scripps Institution of Oceanography, University of California San Diego, La Jolla, CA, USA.

A. Villas Bôas is with the Department of Geophysics, Colorado School of Mines, Golden CO 80401, USA.

II. Measurement technique: principle and practical implementation

A radar interferometer such as KaRIn measures complex radar returns, say s_1 and s_2, at each of its two receiving antennas which amounts to four independent real quantities which can be exploited to reconstruct information about the observed surface. The main combination of interest for KaRIn of these four degrees of freedom is of course the phase difference (often referred to as interferometric phase) between both antennas $arg(s_1 s_2^*)$, which can be processed to reconstruct the topography of the surface [5]–[10]. The individual amplitudes $|s_1|$ and $|s_2|$ can separately be processed into Normalized Radar Cross-Section (NRCS) images of the surface just as in traditional Synthetic Aperture Radar (SAR)

imaging, which in the case of ocean observations at the near-nadir incidence angles and radar frequency band of KaRIn is mainly modulated by wind, with contributions from other processes such as waves, surface currents and the presence of surfactants among others. The SWH measurement that we describe in this paper is based on a fourth independent combination of the two complex radar returns, namely the interferometric correlation

$$\gamma = \frac{|\langle s_1 s_2^* \rangle|}{\sqrt{\langle |s_1|^2 \rangle \langle |s_2|^2 \rangle}} \tag{1}$$

which encodes in a statistical sense the normalized covariance between the two complex signals, and is therefore a real number between 0 and 1. The brackets in equation (1) denote ensemble averages over instrumental noise and ocean surface realizations. We defer the discussion about how these averages are estimated from the data to section II-D and first proceed to describing the various sources of decorrelation.

A. Sources of interferometric decorrelation

Correlation in the context of across-track interferometry has been extensively studied in the literature [5], [6], [11], [12], and can be factorized into various contributions

$$\gamma = \gamma_{SNR}\gamma_{geo}\gamma_{ang}\gamma_{vol}. \tag{2}$$

The first three factors on the right-hand side of equation (2) can be thought of as instrumental sources of decorrelation (although strictly speaking, part of the random noise contributing to the finite SNR comes from surface emission and topography and backscatter gradients contribute to geometric and angular decorrelation). Only the last factor, often referred to as volumetric decorrelation, is impacted by the presence of surface waves. We leave a detailed description of this crucial factor in the context of this work for the next subsection and focus on the instrumental ones here.

The key point of this subsection is that the interferometric measurement provides an estimate of the total correlation γ and that obtaining an estimate of γ_{vol} from which SWH can be inverted first requires estimating these instrumental decorrelation factors. The idea that SWH could in principle be measured using interferometric correlation measurements has been proposed a long time ago, and was present in the original designs of the KaRIn processing chain under a simpler form than what is presented in this paper, namely providing a single SWH value per line of the image, with no cross-track dependance. The main reason for this is that, as we will show in subsection II-B, the inversion in the far range portion of the swath requires an exquisite control of all sources of decorrelation which was not in the mission requirements and therefore could not be guaranteed before launch. This paper demonstrates that such a fine characterization of instrumental effects was indeed achievable through a combination of instrument modelling and monitoring (described in the paragraph below) and static calibration (described in subsection II-C).

The thermal noise part of the correlation γ_{SNR} is simply given by

$$\gamma_{SNR} = (1 + 1/SNR_1)^{-1/2} (1 + 1/SNR_2)^{-1/2}, \tag{3}$$

so estimating γ_{SNR} requires an SNR estimate on each image. This is derived from the total received power $\hat{P}_a$ and a noise-only measurement $\hat{P}_a^{noise}$ performed for each interferometric channel a (1 and 2) before the start of every echo.

$$\hat{SNR}_a = \frac{\hat{P}_a - \hat{P}_a^{noise}}{\hat{P}_a^{noise}}. \tag{4}$$

Throughout the text, hats over quantities denote estimates from the measurements.

The angular and geometric correlation factors are more involved and depend on the point target response (PTR) of the instrument. For the sake of simplicity, we will not provide explicit expressions in terms of the PTR since this would require introducing unnecessary notation, and simply refer the interested reader to section 2 of [5] or Appendix D of [12]. The important point we want to emphasize here is that given the degree of accuracy required, it is crucial to carefully reconstruct the PTR from the radar's internal calibration loop. One important consideration is that the transmitted chirp (and as a result, the range PTR) varies along the orbit, which our dynamical reconstruction from calibration frames allows to capture. Failing to do so would have resulted in very significant (tens of centimeters) errors on SWH which would vary with latitude.

Another crucial effect that we needed to model is the decorrelation created by the conjugate-replica of the received signal generated by tiny imperfections in the local oscillators used for demodulating the echo. The description of this effect is beyond the scope of this paper (see paragraph III.F.6 of [3] for more details) and for the sake of simplicity, we omit it in our equations in this paper (in practice, it is included as a correction to the SNR decorrelation). We simply note that failing to account for this would result in oscillations as a function of the orbital altitude rate with amplitude 10^{-3} in the estimated volumetric decorrelation. Moreover, the phase of these oscillations is related to the along-track Doppler (meaning that the impact is different for the nine Doppler beams formed by the unfocus SAR processing of KaRIn's Low Resolution (LR) mode), making the signature in the beam combined data hard to interpret. This is a perfect example of a dynamical effect that would have been very hard to empirically calibrate and where understanding the root cause and modelling the effect has tremendous added value.

B. Volumetric decorrelation and SWH sensitivity to correlation errors

Several authors have shown that in the presence of ocean waves, γ_{vol} is entirely determined by the height probability distribution (pdf) of the waves. Assuming that this pdf is Gaussian, one readily obtains

$$\gamma_{vol} = e^{-(\kappa SWH)^2/2} \tag{5}$$

where κ is a geometric coefficient proportional to the ratio of the interferometric baseline (approximately 10 m for SWOT) and the cross-track distance. Again, to avoid unnecessary notation, we refer the reader to [12], [13] for explicit expressions of κ in terms of different geometric parametrizations. The

left panel of Figure 1 shows γ_{vol} as a function of cross-track distance for different values of SWH. The first obvious observation is that $\gamma_{vol} = 1$ in the absence of waves (no decorrelation) and then decreases as SWH increases: higher waves introduce more decorrelation as an increasing number of points on the (wavy) surface coincide in range. As one moves away from nadir, i.e. as cross-track distance increases, γ_{vol} asymptotically approaches 1, meaning that the decorrelation from the waves becomes weaker. Crucially, the curves for different SWH are much more separated in the near range than they are in the far range, meaning that the sensitivity to SWH is very poor in the far range. The right panel of figure 1 quantifies that sensitivity by showing the (absolute) SWH error resulting from a fixed error in the γ_{vol} measurement, i.e. assuming that we measured $\hat{\gamma}_{vol} = \gamma_{vol}(1 - \epsilon)$. Note that we use the term error here to denote any source of discrepancy between the measured and the true volumetric decorrelation, be it from random fluctuations (e.g. caused by thermal noise) or from possible systematic errors in the determination of the other sources of decorrelation (e.g. from a systematic error in the PTR reconstruction). The SWH bias is a function of both the cross-track distance and the true SWH itself. The figure shows the bias as a function of the true SWH for three cross-track distances : near-nadir edge of the swath (10 km, blue), center of the swath (35 km, green) and far-range edge of the swath (60 km, orange). The various values of ϵ used in the figure are positive, corresponding to overestimates of SWH. Negative values would of course result in underestimates of SWH, but we note that given the non-linear relation between γ_{vol} and SWH, changing the sign of ϵ would also result in slightly different absolute biases, especially at low SWH. For the sake of space however, negative values of ϵ are not shown but we keep the discussion generic in terms of absolute bias. The absolute bias is a decreasing function of the true SWH. In other words, it is actually easier to provide accurate estimates in the high SWH regime. In the near range, an error of 10^{-3} on decorrelation translates to a SWH bias of the order of centimeters or less throughout the entire SWH range (solid blue line). In the far range, by contrast, the same error on decorrelation already leads to tens of centimers worth of error in SWH (solid orange line), meaning that our knowledge of all instrumental sources of decorrelation has to reach an accuracy better than 10^{-3}. The dashed curves show the absolute bias assuming an order of magnitude reduction in the error on γ_{vol}, i.e. $\epsilon = 10^{-4}$. In that case, the SWH bias remains below 10 cm except for very low values of SWH throughout the entire swath.

C. Calibration of the decorrelation measurement

In order to achieve an accuracy of the order of a few 10^{-4} on the instrumental sources of decorrelation, we complement the modelling of these sources (see subsection II-A) with a calibration procedure that we describe here. The idea behind this is that given the high accuracy required, it is crucial to correct for potential residual errors in our characterization of the known sources of decorrelation and also to capture potential sources of decorrelation not included in our modelling. We emphasize from the beginning that we were able to restrict ourselves to a purely static[1] calibration of volumetric decorrelation (not SWH) which can be derived offline once and for all from a few hours of SWOT data (using both data from KaRIn and from SWOT's nadir instrument) and then applied on the KaRIn data regardless of whether the nadir instrument is operating or not. In other words, the SWH from KaRIn is in no way dynamically adjusted to the nadir SWH.

In practice, the calibration is derived as follows. We first select 40 passes of KaRIn data (about one and a half days in total; the only criterion for the selection at this stage is that they are mostly over ocean, to maximize the amount of useful data) and chunk them into 50 km segments in the along track direction. Only segments where all pixels have their quality flag set to good, which are entirely over the ocean, and whose latitude is below 50° in absolute value (to avoid ice) are kept. We also reject segments where the σ_0 drops by more than 4dB below the segment median, in an attempt to avoid rain contaminated data. This leaves us with a collection of about 4800 segments (the equivalent of about half a day of KaRIn acquisitions if they had been collected continuously) for each swath which we actually use for the calibration. Each swath corresponds to a different polarization of the transmitted and received radar signal (note that the correspondance between left/right and H/V depends on whether the spacecraft is yaw-flipped or not, see section 3.1.14 of [14]) and is therefore potentially affected by slightly different errors in our modelling of the instrumental sources of decorrelation. As a result, we derive one calibration for each polarization independently. We also note that we require slightly different calibrations for the so-called CAL orbit (1-day repeat orbit used during the first 6 months of the mission) and the SCIENCE orbit (21-day repeat orbit used for the rest of the mission). While the calibration procedure is exactly the same for both orbits, we only show the results for the CAL orbit here for the sake of space.

Without any calibration, our volumetric decorrelation estimate would simply be

$$\hat{\gamma}_{vol} = \frac{\hat{\gamma}}{\hat{\gamma}_{SNR}\hat{\gamma}_{geo}\hat{\gamma}_{ang}} \tag{6}$$

where all quantities in the right-hand side are either direct measurements or the result of reconstructions using our in-

[1]During the last stages of the review process for this paper, we have started gathering evidence that the instrumental effects captured by the (currently static) calibration vary over long timescales (likely controlled by the angle β between the vector from the Earth to the Sun and the plane containing the spacecraft orbit around the Earth, which affects the solar illumination of the spacecraft and therefore influences the thermal environment of the SWOT spacecraft and its instrument [14]; this angle follows a cyclic pattern with a timescale of months in the case of SWOT). So far, the observed deviations with respect to the static calibration derived here and shown in Figure 2 are smaller than $2\,10^{-4}$ for most of the range of β angles, but can reach up to $4\,10^{-4}$ for the largest values of $|\beta|$. In those situations, biases larger than the ones shown in this paper, e.g. in Figure 11, can appear (up to several tens of centimeters at low SWH in the far range). Confirming and fully characterizing these residual errors will require significantly more data, which will become possible when the entire dataset of SWOT observations (from the beginning of the mission up to now, which represents several beta cycles) gets reprocessed with the version of the algorithm described in this paper (version D of the products). We leave a description of these errors and of algorithm evolutions designed to correct for them for future work.

This article has been accepted for publication in IEEE Transactions on Geoscience and Remote Sensing. This is the author's version which has not been fully edited and content may change prior to final publication. Citation information: DOI 10.1109/TGRS.2025.3551605

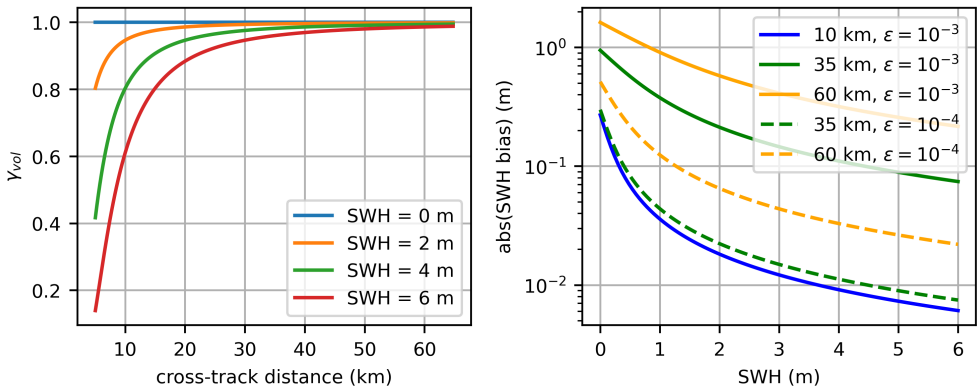

Fig. 1. Volumetric decorrelation as a function of cross-track distance for various SWH (left panel). Absolute SWH bias (in log scale) caused by various levels of error on the volumetric decorrelation estimates parameterized by ϵ (solid vs dashed lines) and for various cross-track distances (colors) as a function of the true SWH (right panel). The impact of a fixed error in the decorrelation measurement ϵ drastically increases at low SWH and towards the outer edge of the swath.

strument models and monitoring measurements (noise power, range PTR, etc...). The previous equation applies for each pixel of each segment (which is composed of 200 along track samples, or lines, and 240 columns, or across-track samples since we work with the native posting and resolution provided by the On-Board Processor (OBP), namely 250 m and 500 m respectively) but in order to simplify the notation, we will omit all line and column indices. Additionally, the terms in the right-hand side in principle depend on the Doppler beam formed during azimuth compression. To keep this discussion simple, and since our calibration is derived on the beam-combined volumetric decorrelation anyway, we omit the beam dependance here (but it is of course accounted for in the actual calibration procedure).

Our calibration scheme consists in replacing equation (6) by

$$\hat{\gamma}_{vol}^{cal} = \frac{\hat{\gamma}}{\hat{\gamma}_{SNR}^{cal}\hat{\gamma}_{geo}\hat{\gamma}_{ang}\gamma_{cal}} \tag{7}$$

where the only modifications are the inclusion of a calibration for the SNR and the introduction of a γ_{cal} factor in the denominator. More explicitly, we allow for a multiplicative SNR calibration of the type

$$\hat{SNR}^{cal} = \hat{SNR}\,(1+\eta) \tag{8}$$

where η is a small constant scalar value (while it could in principle be polarization dependent, we find that a single value common to both is sufficient). In other words, for each KaRIn pixel (regardless of its along- and across-track position or Doppler beam), we simply first rescale the measured SNR with the same real number $1+\eta$ before computing the associated SNR decorrelation using (3). In addition to this, we introduce a static calibration factor γ_{cal} at the decorrelation level, which we allow to depend on the cross-track distance. In other words, for each polarization, we need to determine an across-track calibration profile (one real value per 250 m cross-track bin, i.e. 240 values in total). Note that the assuption that such a static calibration is sufficient to control all sources of instrumental decorrelation to the required level was not *a priori* guaranteed, since those errors could in principle vary with time (for instance due to variations of instrumental parameters at the orbital timescale). Below, we show that this is indeed sufficient, which was made possible by refining our instrumental models to capture the main dynamical effects. Had this not been the case, an emprical calibration of these dynamical effects would have been necessary and we note that this is a very hard problem: as long as the root causes of the dynamical variations have not been understood, even just identifying the proper variables on which the calibration should depend can be extremely complex given the non-linear nature of the phenomena at play.

The goal of the calibration procedure is therefore to derive optimal values for γ_{cal} as a function of cross-track distance and for the parameter η, which we do by using the SWH provided by SWOT's nadir instrument as ground truth. Specifically, for each pixel of each segment, we compute a "ground truth" value for $\gamma_{vol}^{truth} = \gamma_{vol}^{theo}(SWH_{nadir})$ by injecting the 1HZ MLE4 nadir SWH (interpolated to the time of the KaRIn measurement) into equation (5). For each segment, we compute a cross-track profile of $\hat{\gamma}_{vol}/\gamma_{vol}^{truth}$ by simply talking the median over each cross-track bin. Finally, for each cross-track bin, γ_{cal} is defined as the median over all segments of the ratios $\hat{\gamma}_{vol}/\gamma_{vol}^{truth}$. Given the fact that the measurements by KaRIn and the nadir are not colocated (with separations of up to 60 km in the far range portion of the swath, over which the SWH often varies significantly), one important assumption behind our calibration strategy is that, on average, both are the same. In other words, we assume that both the nadir noise and the difference in measurement location only contribute to the width of the distribution of $\hat{\gamma}_{vol}/\gamma_{vol}^{truth}$ but do not affect its median. This procedure requires that the calibrated SNR is used in the determination of $\hat{\gamma}_{vol}$, which requires choosing a value of η. A range of values has been explored, and we observed that deviations from $1+\eta = 0.15\text{dB}$ (i.e. $\eta \approx 0.035$) very quickly lead to an unphysical curvature of $\hat{\gamma}_{vol}$ in the far range (a small error in the SNR translates into a large error on SNR decorrelation in the far range because the SNR is smaller there). This is therefore the value that we adopted

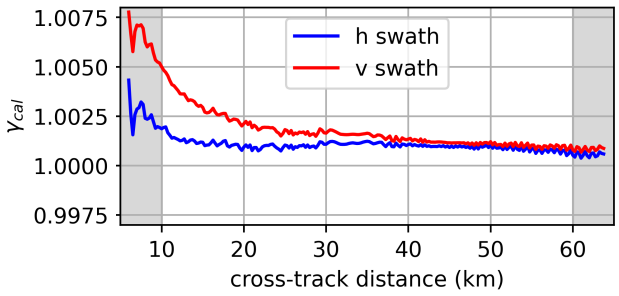

Fig. 2. Static calibration profile of volumetric decorrelation as a function of cross-track distance for each polarization. The shaded gray areas on each side show the portions of the swath beyond requirements. This static calibration is designed to correct for errors in our modeling of known instrumental sources of decorrelation and to capture potential additional sources of decorrelation not accounted for in our models.

for our SNR calibration. Such a small discrepancy could be attributed to various factors such as the frequency response of the receiver on the noise estimate. The final profiles for γ_{cal} are shown in Figure 2.

On top of allowing us to fix the calibration parameters, the procedure described above provides us with an entire distribution of $\hat{\gamma}_{vol}^{cal}/\gamma_{vol}^{truth}$ for each range bin, sampling a variety of instrumental, orbital and observed surface configurations. This can be used as a first way of investigating whether our static calibration is sufficient, by checking how the median of $\hat{\gamma}_{vol}^{cal}/\gamma_{vol}^{truth}$ computed over bins in these various parameters behaves. This is shown in Figure 3 for a cross-track distance of 60 km, i.e. at the far range edge of the swath where, as explained in subsection 3, we need the most accurate estimates of volumetric decorrelation. Each panel shows the dependence on a different parameter: orbit altitude (H) and altitude rate (dH/dt) in the top row, σ_0 (the median of the NRCS measured by KaRIn over the entire segment is used) and SWH (median of the nadir measurements over the segment) in the bottom row. The histograms in the background show the distribution of the parameter of interest among our collection of segments[2], providing some insight as to which portions of parameter space are less statistically reliable for this analysis. The solid lines represent the median of $\hat{\gamma}_{vol}^{cal}/\gamma_{vol}^{truth} - 1$ computed over each bin of the histogram. For our static calibration to meet our needs, this quantity should remain of the order of 10^{-4} across the entire parameter space, which is indeed the case. Initial attempts using a static calibration on top of less refined models of the instrumental dynamical behavior featured oscillations and trends as large as a few times 10^{-3}.

We emphasize that the approach taken in this work is not to look for an empirical calibration of SWH that would take sea state parameters as inputs. Rather, we derived an empirical calibration (depending on purely instrumental parameters such as cross-track distance and polarization) of the instrumental effects that impact our conversion from the total correlation that we measure to the volumetric correlation that we want to invert on a physical basis using equation (5).

[2]We note that the sampled altitude distribution does not cover the entire range of the CAL orbit due to our restriction in latitude to avoid sea ice in our calibration dataset. Similarly, values of SWH smaller than 50 cm or larger than 5 m and values of σ_0 different from 14dB by more than 2dB are barely sampled in our dataset.

D. SWH inversion algorithm in practice and illustration

The SWH inversion algorithm from the (calibrated) volumetric decorrelation estimates obtained through equation (7) is straightforward. One important thing to keep in mind is that this equation applies to the 250 m-posting/500 m-resolution pixels formed after averaging by the on-board processor, which is the only data that is downlinked to the ground and available for processing. We note however that equation (5), which is derived from (1), is in principle valid at the level of the single-look complex (SLC) pixels, i.e. prior to on-board averaging. Indeed, the brackets in equation (1) denote ensemble averaging over instrumental noise realizations as well as over small scale scatterer distribution (leading to speckle) and surface wave realizations given a sea state (i.e. a value for SWH in this context). In practice, these expectation values are replaced by local averages of the (flattened) interfereogram and powers computed using the on-board filters defined in [8]. In other words, the OBP conveniently provides us through its averaging step with estimates of the expectation values of the SLC conjugate products entering the definition of statistical correlation, and our total correlation estimate appearing at the denominator of (7) for each OBP pixel is simply the ratio between the interferogram magnitude and the square root of the product of the powers for this individual pixel. Such a simple statistical estimator of coherence is known to be biased [15], [16], with larger biases for small γ and small number of looks. In the case of SWOT, the number of looks within any OBP pixels (with 500 m resolution in both directions) is large, and we do not explicitely account for this effect (whose average value over all observation conditions should additionally be captured by our static calibration).

The only degree of freedom that we introduce in our algorithm is the resolution at which the inversion is performed. We leave the full characterization of the fluctuations of $\hat{\gamma}_{vol}$ around its expectation value caused by instrumental random noise as well as variability in the waves realization (given SWH) for future work, but we note they often cause the estimate to overshoot the maximum physical value of 1, leading to no solution in the inversion. Already for this reason, it is clear that at least some amount of local averaging of the volumetric decorrelation estimates themselves in order to reduce the variance of the fluctuations before using (5) leads to a better behaved inversion. The scale used for averaging should then be guided by the usual trade-off between the scale of the spatial modulations of the SWH that one aims at capturing and the amount of noise in the estimates that one is willing to accept.

As we will argue in section III, the latter is hard to characterize, and we refer the reader to that section for a full discussion of the measurement error and upper bounds on the measurement noise. Geophysically, SWH varies at a broad range of scales. At oceanic mesoscales (100-10 km), the spatial variability of SWH is mostly driven by wave-current

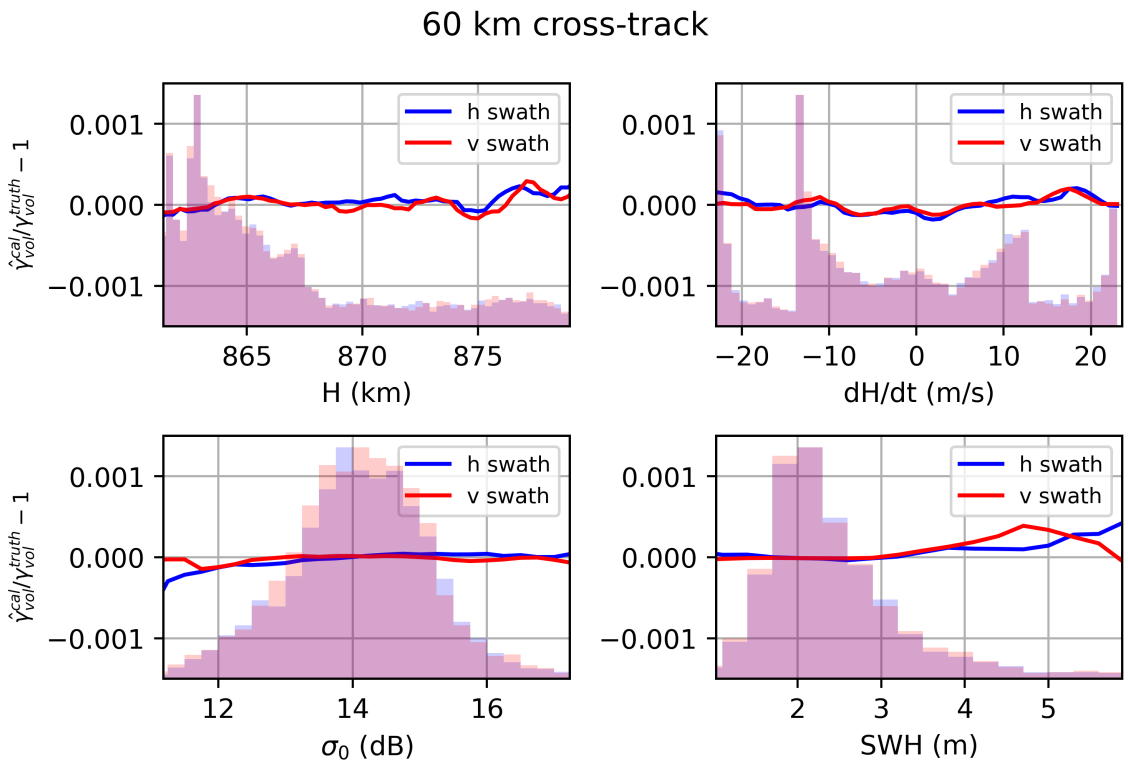

Fig. 3. Stability of the median ratio between the calibrated volumetric decorrelation estimate from KaRIn and the one computed from the nadir SWH as a function of various orbital and surface parameters. The figure is for the cross-track bin at the far-range edge of the swath, corresponding to a cross-track distance of 60 km, where maximum accuracy is required. Our modelling of instrumental effects augmented with the static calibration described in this section are sufficient to keep the magnitude of the deviations at the 10^{-4} level.

interactions [17]–[21]. However, as we approach scales on the order of a few kilometers, wave groups start to play an important role in the SWH variability, especially in swell-dominated cases [22]. In practice, the modulations of the wave envelope give rise to random fluctuations in the local SWH (defined as four times the standard deviation of surface heights over a spatial window) whose standard deviation depends on the background SWH, the peakedness of the wave spectrum and the size of the window. To capture the full range of scales of variability in SWH, we chose to consider two different resolutions for our inversion, namely 2 km and 5 km. The main driver behind the choice of a scale as small as 2 km is consistency with the SSH resolution of KaRIn products, with the idea of eventually factoring the retrieved SWH fields into a sea state bias correction.

Practically speaking, this means that we first filter $\hat{\gamma}_{vol}$ in along-track with a 2 km or 5 km long kernel. In the cross-track direction, in order to account for the dependence of volumetric decorrelation on incidence angle (even at constant SWH, see figure 1), we replace the filtering by a least squares fit over 2 km (or 5 km) intervals. While this makes a small difference at the 5 km resolution, this is negligible at 2 km resolution and the operational algorithm in KaRIn's ground processing, which only provides 2 km-resolution estimates, uses a simple cross-track averaging instead of this piecewise fits. Note that any 250 m pixel flagged as rain-contaminated, land or ice is discarded prior to the averaging (or cross-track fit).

Figure 4 illustrates the result of the SWH inversion on an example from cycle 481 and pass 16, where a strong diagonal feature associated with the presence of currents is seen (the physics of this example will be discussed in more details in section IV). The one-dimensinal collection of points between the two swaths are the 1Hz measurements from SWOT's nadir altimeter. A global comparison between the nadir and KaRIn's measurement will be presented in section III-D, but this example already illustrates the excellent agreement between the two (if one considers the near range part of KaRIn's swaths of course). The nadir also sees the strong positive SWH anomaly at the location where it intersects the nadir track, but the KaRIn two-dimensional measurements reveal its actual shape and orientation, providing a much more complete picture of the phenomenon.

III. Validation against independent observations

In this section, we validate the SWH measurements obtained with the method described in section II against several independent sensors.

A. CSIRO GPS moored buoy

The Southern Ocean Time Series (SOTS) mooring GNSS data contains in situ observations of the sea surface for each yearly deployment of the mooring since 2019 (-47°, 141°). The mooring is located in the right swath of SWOT's pass 19

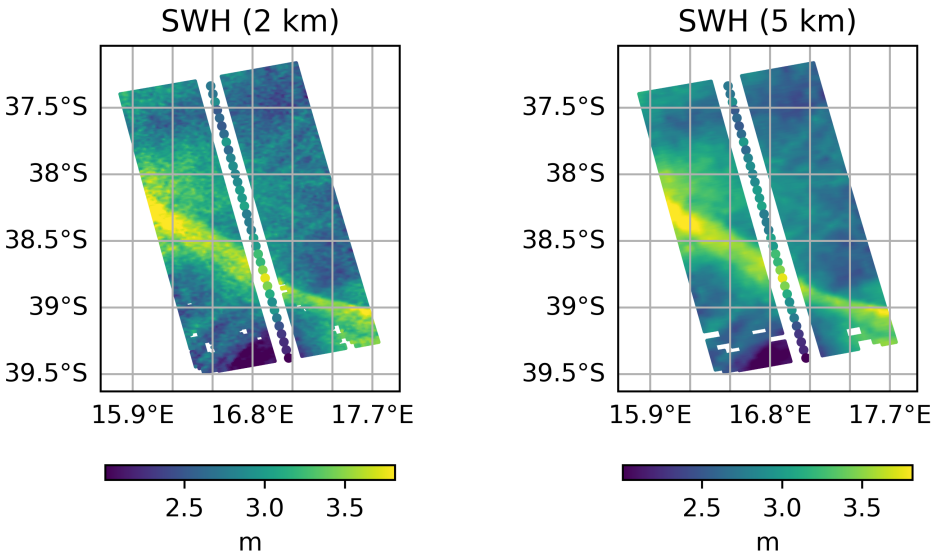

Fig. 4. Illustration of the KaRIn SWH inversion at 2 km and 5 km resolution on an example in the Agulhas current (cycle 481, pass 16). The gaps visible in both swaths between 39°S and 39.5°S are due to an editing algorithm aiming at rejecting rain contaminated areas based on local NRCS drops.

of the 1-day repeat CAL orbit (at about a 30 km cross-track distance), providing us with a timeseries of colocated SWH measurements between KaRIn and the buoy starting from the end of SWOT's commissioning phase (March 31st, 2023) and ending at the end of SWOT's 1-day repeat phase (July 9th, 2023). The SWH from GNSS is determined by first processing the observations using GipsyX [23] using kinematic precise point positioning to give positions at 2 Hz with centimeter level accuracy. From this, the SWH is calculated [24] as 4 times the standard deviation of the height component over a rolling window of specified length (90 minutes for the data used in this comparison).

The top panel of figure 5 shows the SWH timeseries from the buoy (black) and KaRIn (blue and red for 2 km and 5 km resolution respectively). For certain days (8 out of the 96 in the entire period), the comparison was not possible, either because the buoy was in a rain contaminated area which was edited in KaRIn's processing (and the closest valid measurement was several kilometers away), because of data gaps in KaRIn's raw data (from May 20th to May 22nd included), or because the buoy data was not available (from May 15th to May 17th included). The nadir measurements (green) are also provided for comparison, but it is important to keep in mind that they are not colocated with the buoy (the nearest 1Hz point was used) and the geophysical spatial variability in the SWH field can be a significant contribution to the measured differences. Given the mooring location in the Southern Ocean, a wide range of SWH values (up to almost 10 m) is sampled. The panel in the second row shows the SWH differences between SWOT and the buoy for each day while the third row features histograms of those differences. We refer the reader to section III-E for a more thorough discussion about measurement error for the KaRIn SWH, but the histograms in Figure 5 already provide a first indication in the form of an upper bound since any error in the in-situ data would also contribute to the measured differences.

More importantly, the buoy SWH are computed from the height variance within a 90 minute window, which introduces some smoothing of the wave group modulations that propagate through the buoy location during that time, and of which KaRIn captures a frozen snapshot. In order to illustrate the differences that can be introduced by this inconsistent sampling of wave groups between both instruments alone (even in the absence of any instrumental error), we focus on one example, namely cycle 556 (corresponding to June 19th; this is one of the most extreme cases in our timeseries where the measured SWH was above 9 m and the difference between KaRIn and the buoy reaches 69 cm at 2 km resolution and 24 cm at 5 km resolution). Starting from the wave spectrum provided by the WaveWatch3 model (at the closest model grid point from the buoy location), we numerically generated random realizations of discretized sea surfaces and evolved them in time to simulate the buoy and KaRIn sampling of the surface. Simulated buoy SWH measurements were constructed by computing (four times) the standard deviation of the elevation of a single grid point within a 90 minute window, whereas the KaRIn-like sampling was mimicked by taking (four times) the standard deviation of elevations within a 2x2 km (or 5x5 km) square box centered on the buoy location, with the surface generated at a time corresponding to the center of the 90 minute window. We emphasize that no instrumental noise was introduced in the simulation, since our goal here was to evaluate the contribution from differences in surface sampling only. Using a large number of different random seeds, this procedure allows for a Monte Carlo estimation of the standard deviation of the difference in SWH measurements due to the difference in the way both instruments sample the random group fluctuations, which in this example was 35 cm and 26 cm for the 2 km and

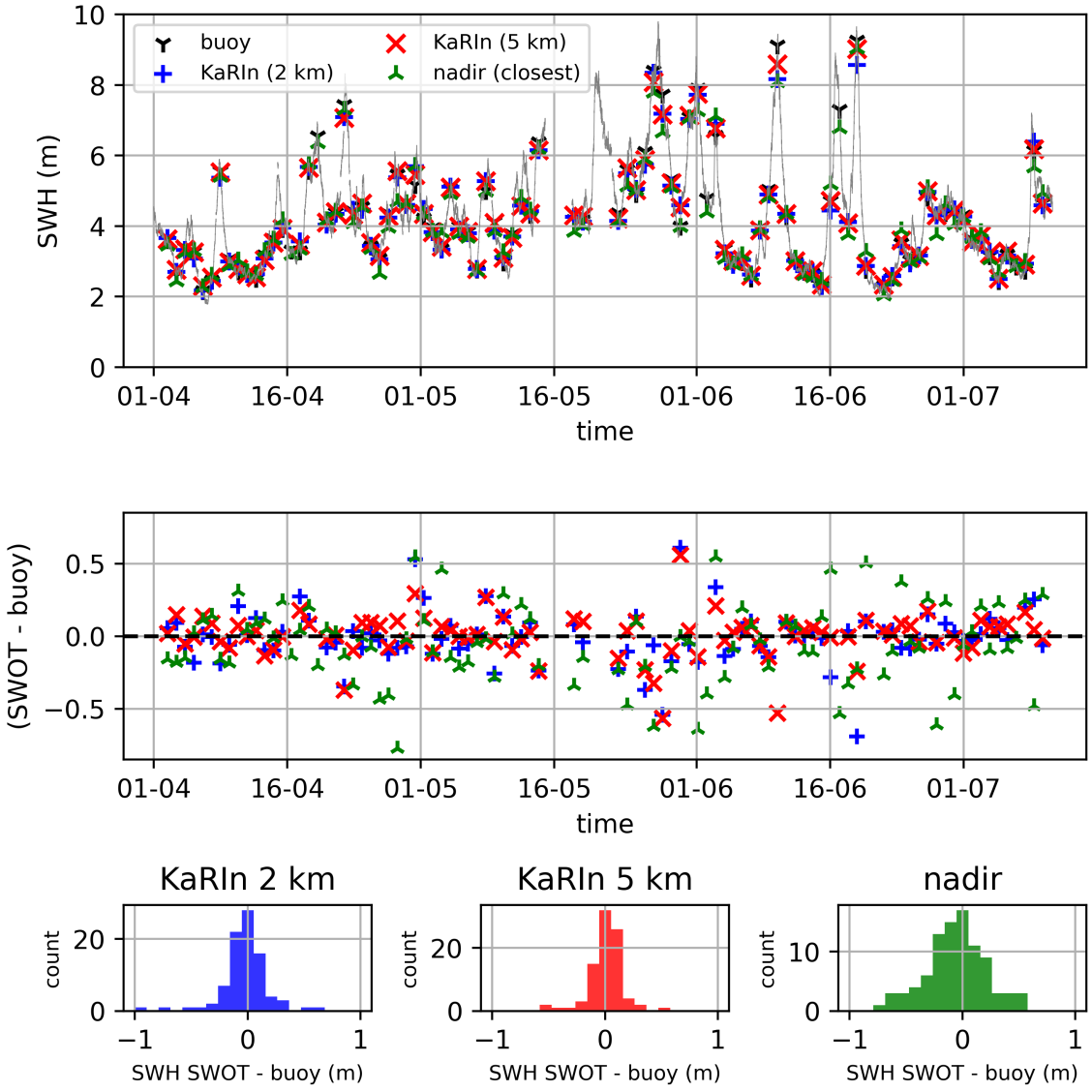

Fig. 5. Comparison between the SWH measurements from the buoy and from SWOT. Top panel: SWH timeseries for each instrument (two different resolutions used in the processing of KaRIn data). The location of the buoy in the Southern ocean allows to sample a wide regime of SWH. Middle panel: timeseries of differences between the SWOT measurements and the ones from the buoy. Note that the measurements between KaRIn and the buoy are exactly colocated in space and time, but a 90-minute window is used to estimate SWH from the buoy data, possibly smoothing some of the smallest structures such as wave group modulations travelling through the area during this period. The observed differences are a combination of KaRin measurement noise, noise in the buoy measurement itself, and this discrepancy in the length of the observation. The nadir measurement is not colocated in space with the buoy, which lies almost at the center of the swath. Histograms of the differences are shown in the bottom panel. Their width provides an upper bound of KaRIns measurement error.

5 km KaRIn measurements respectively. In other words, the difference of 69 cm between KaRIn (2 km) and the buoy in this case is of the order of a 2σ fluctuation from group sampling alone. Of course, the measured difference actually receives contributions from instrumental noise as well, and separating the sampling contribution from the instrumental contribution is not possible on a single example. We leave for future work a statistical analysis aiming at separating both, which would require accumulating a statistically significant population of cases with similar levels of instrumental noise and of sampling noise. For now, we simply wanted to illustrate that group sampling is an important contribution to the KaRIn vs buoy differences. As a consequence, the standard deviations (15 cm at 5 km resolution and 20 cm at 2 km resolution) obtained from the histograms of differences cannot be interpreted in terms of instrumental error. The small mean bias shown in these histograms of differences underscores that KaRIn is giving accurate SWH measurements throughout the wide range of SWH sampled by the buoy.

B. Airborne remote sensing observations from MASS

We now compare KaRIn's SWH measurements to independent data acquired by the Modular Aerial Sensing System (MASS) [25], [26] during the MASS-SWOT post-launch Cal-Val campaign in April and June 2023, where 13 flights were scheduled to match SWOT's observation time. The MASS

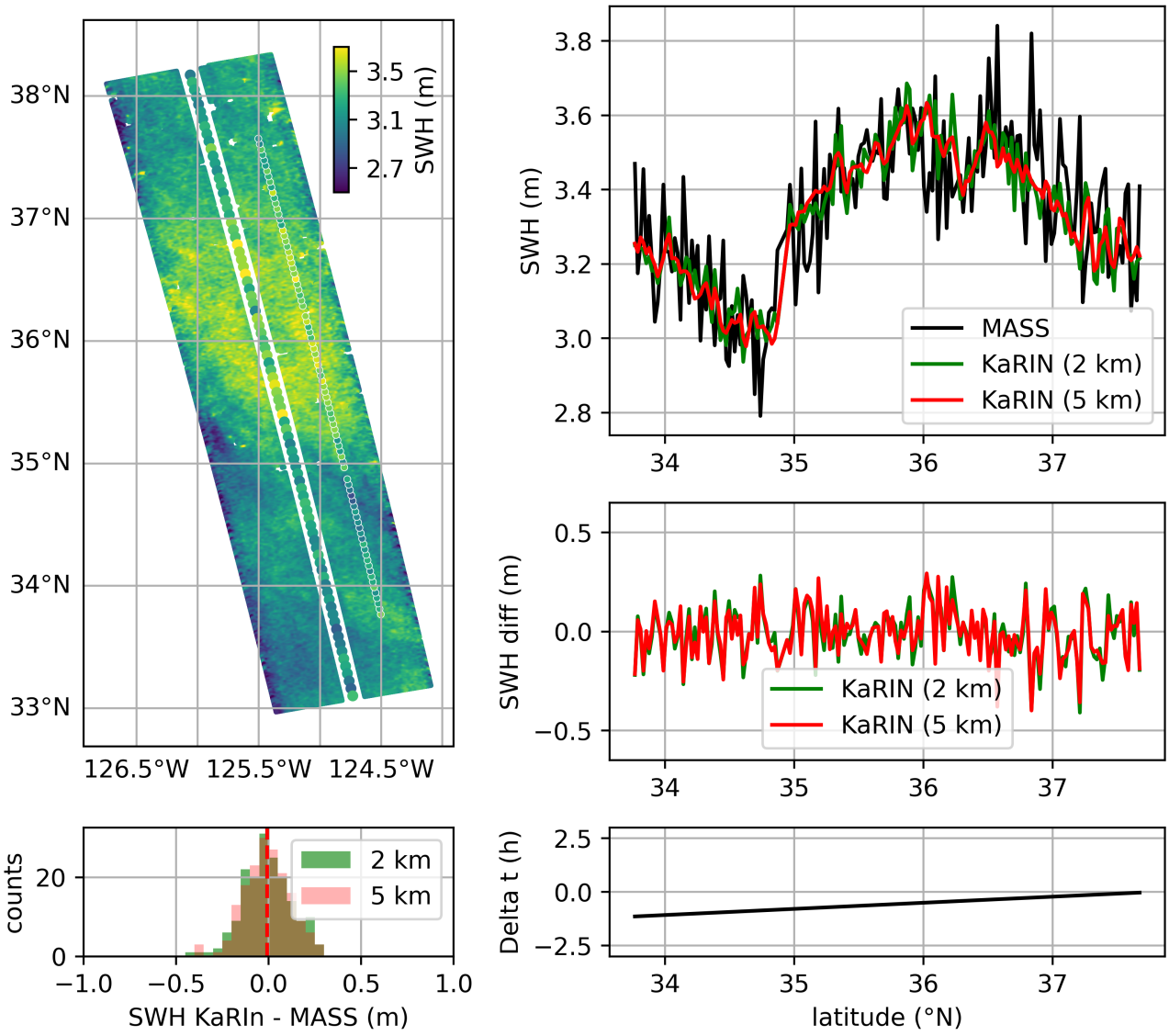

Fig. 6. Comparison between KaRIn and MASS for the flight of April 3rd. Top left panel : 2D SWH map from KaRIn, SWOT's nadir measurements between the swath and the measurements from MASS (markers with white contours; for this panel only, only one in every two MASS measurements is shown to improve readability) overlaid on top of KaRIn's swath. The 1-dimensional profiles of SWH along the MASS track are shown in the top right panel, and the KaRIn-MASS differences in the middle right panel. Small scale features like the sharp gradient at 35°N are captured coherently by both instruments. Histograms of the KaRIn-MASS differences are shown in the bottom left panel. Their width is a very loose upper bound on KaRIn's measurement noise since most of the high frequency fluctuations come from MASS's sampling of the wavy surface at 0.5x2.5 km. The bias between both instruments is centimetric. Bottom right : difference in observing times between MASS and KaRIn along the profile. The aircraft carrying MASS takes about an hour to complete this profile. Flights with larger separations in time with SWOT's measurement typically result in larger differences, illustrating that temporal variability at the scale of a few hours is non negligible.

instrument is built around a Q680i waveform scanning lidar (Riegl, Austria), used to make spatiotemporal measurements of the sea surface elevation, combined with detailed collocated and coincident optical observations (visible, infrared and hyperspectral). The SWH from MASS is estimated [26] from the lidar point cloud returns as 4 times the standard deviation of surface height within boxes of approximately 500 m (fixed by the instrument's swath) by 2.5 km.

Figure 6 provides an example of comparison between MASS and SWOT for the MASS flight of April 3rd, 2023 (corresponding to cycle 479 and pass 26 for SWOT). This particular flight was divided into 4 repeating legs cutting an along-track profile of KaRIn's right swath (this corresponding to a descending orbit for SWOT, the left swath under the terminology of [14] is on the right on our plot) at a cross-track distance of about 35 km. One important factor to take into account in this comparison is the fact that the wave field evolves over the several hours required for the flight. A common pattern observed in all flights is that the discrepancies in the observed SWH between MASS and KaRIn tend to increase with the difference in observing times, with noticeable differences of several centimeters over the timescale of hours.

For this flight, each leg takes slightly above one hour to complete (with SWOT's observation time coinciding almost exactly with the transition between legs 2 and 3) and the figure uses the second leg of MASS data, i.e. the one acquired during the hour just before SWOT's acquisition (a figure using the third leg, acquired in the hour just after SWOT) would have looked very similar.

The two-dimensional SWH image from KaRIn (only shown at 2 km resolution for the sake of space) is shown in the top left panel, together with the nadir measurements (disk markers between both swaths). The scene features strong spatial modulations of SWH, with variations of several tens of centimeters over only a few tens of kilometers. Overlaid, with white contours are the MASS measurements. In order to appreciate the excellent agreement, the one dimensional profiles of SWH along MASS's leg are shown in the top right panel as a function of latitude. Features like the sharp gradient just south of 35°N (more than 30 cm over about 30 km) are captured very similarly by both intruments, suggesting that they are indeed physical and illustrating KaRIn's ability to probe fine scales in the SWH field.

The differences between MASS and KaRIn are shown in the middle right plot and look almost identical for the 2 km and 5 km resolution. As could already be seen in the top plot, most of the high-frequency fluctuations come from the MASS measurements, predominantly coming from statistical fluctuations in the local SWH (e.g. from wave groups) defined at the scale of MASS's averaging window[3], which is limited to 500 m in the across-track direction. We leave a more quantitative investigation of those fluctuations for future work, and simply point out that the MASS-KaRIN rms difference of 15 cm at 2 km resolution and 14.5 cm at 5 km resolution is an upper bound on KaRIn's measurement noise. The histogram of the differences between MASS and KaRIn (medians of each distribution in dashed and very close to zero) in the bottom left plot however indicate that the relative bias between both instruments is very small, at least in this regime. The bottom right plot indicates the difference in observing times between MASS and SWOT along MASS's leg.

Figure 7 provides a summary of the comparison between MASS and KaRIn over the entire MASS campaign, keeping only the collocated measurements with less than 1h between the observation times and using a very basic editing step (removing outliers with differences of more than 1.5 m) to get rid of corrupted lidar data caused by cloud contamination. For context, the distribution of SWH values sampled by this dataset (2970 points in total) are shown in the top right plot. The top left panel shows the histogram of the SWH differences between KaRIn and MASS. The medians of the distributions are -1 cm for both the 2 km and 5 km resolutions, confirming the very small bias between MASS and KaRIn already seen on the example of the April 4th flight. We note that the distributions of SWH differences show a small tail with negative values between 50 cm and 1 m (which slightly push the means of the distributions to negative values, namely -2 cm and -3 cm for 2 km and 5 km). This tail is caused by a couple of legs where MASS was flying towards the edge of KaRIn's swath, at cross-track distances very close to 60 km and at a time where the waves were low (true SWH of about 1 m), which is precisely the region of parameter space where small errors on volumetric decorrelation translate into large errors on SWH. In a histogram where only cross-track distances smaller than 55 km are used (not shown here for the sake of space), the tail disappears and the mean bias between KaRIn and MASS gets reduced to below 1 cm. The bottom row shows histograms of SWH differences for different cross-track distance bins, with nicely centered distributions throughout the swath except at the very edge (rightmost plot) where the negative bias is visible. A more global investigation of KaRIn's errors as a function of cross-track distance is is presented in sections III-D and III-E. The negative bias observed here is not seen at a global scale (rather, a small positive bias, dependent on SWH itself, is observed against SWOT's nadir). The most likely explanation for this is that in the very far range a small dynamical error in our modeling of decorrelation of instrumental origin remains (for instance from an imperfect PTR reconstruction) and creates an error in SWH which varies along the orbit (with possible systematic contributions) and happens to be mostly negative over the dataset used in this section.

To conclude this comparison between MASS and KaRIn, we emphasize that the width of these distributions (respectively 22 cm and 24 cm for the 5 km and 2 km resolutions in the top left plot) cannot be easily related to KaRIn's random measurement error in SWH, since other factors like temporal evolution of the SWH field between the acquisitions and the different filtering of very small scale modulations (groups) by both instruments due to the geometry of the acquisition also contribute to the observed differences.

C. Cross-over with Sentinel 3

Figures 8 and 9 show an example of cross-over between SWOT (cycle 540, pass 24) and Sentinel 3A (S3A) with a difference in acquisition times of slightly less than 3 hours. In both figures, the left panel shows the two-dimensional SWH field retrieved by KaRIn at 2 km resolution, together with SWOT's nadir measurement (dots between KaRIn's swaths) and S3A's 1Hz measurements in SAR mode (markers with white contours). Figure 8 shows the intersection of S3A with the left (right on the plot since this is a descending orbit) swath of KaRIn. The scene features a very smooth North-South gradient going from less than 2 m to more than 3 m, which is well captured by all instruments. The central panel shows the S3A profile of 1Hz measurements (black) as well as the KaRIn measurements (at 2 km resolution in green and 5 km resolution in red) reinterpolated onto the S3A measurement locations to provide a more quantitative way to assess the agreement. Finally, the right panel shows the difference between KaRIn and S3A along the S3A profile,

[3]The statement that the fluctuations in the MASS SWH mainly come from sampling rather than from instrumental noise is supported by performing simulations of random realizations of sea surface from the WaveWatch3 wave spectrum corresponding to the location and time of the flight and computing standard deviations within boxes of 0.5x2.5 km. Those show similar levels of fluctuations as the high frequency variations in the MASS data.

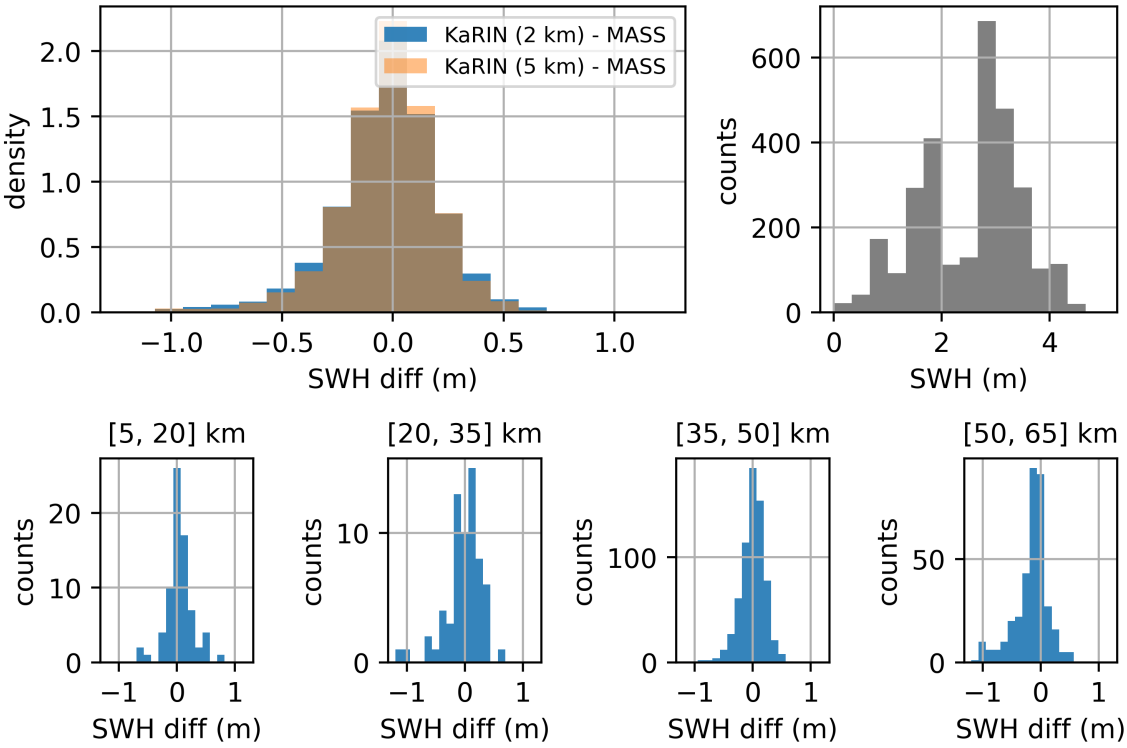

Fig. 7. Summary plots for the comparison between KaRIn and MASS over the entire campaign of CalVal flights. Only measurements within one hour have been kept to limit the impact of temporal variability of the wave field. Top right : histogram of the SWH values sampled through the campaign, for context. The full histogram of KaRIN-MASS differences is shown in the top left panel. The median bias (for both resolutions) is -1 cm. Again, the width of the histograms cannot be directly interpreted in terms of KaRIn measurement noise since it receives contributions from MASS's noise and, predominantly, from the difference in the way both instruments sample the random fluctuations from wave groups at very small scales. These global histograms of differences are broken down by cross-track distance bins in the bottom row (note the different sample sizes between the histograms). Median biases remain very close to zero throughout the swath, but do increase slightly at the edge of the swath, where the measurement is most sensitive to errors. This far range error is most likely due to systematic errors in the modelling of instrumental sources of decorrelation (at the level of 10^{-4}) and therefore actually latitude dependent. See the discussion in section III-E for more details.

with deviations typically bellow 10 cm, in particular in the southernmost part of the segment.

Figure 9 shows the Northern portion of the cross-over, where S3A crosses the left swath of KaRIn. While the mean SWH value is similar to that of Figure 8, with a negative North-South gradient, the measurements from all instruments show much more high-frequency content, which is due to the presence of wave groups [27]. To confirm this, we computed the two-dimensional spectral peakedness Q_{kk} introduced in Eq. (4) of [22] and which controls the amplitude of the local SWH modulations from the groups from WaveWatch3 spectra corresponding to the center of each segment ($15.5°S$ and $25°S$ respectively). The scene in figure 9 ($Q_{kk} = 44$ m) does indeed correspond to a noticeably narrower spectrum than the one in figure 8 ($Q_{kk} = 18$ m) and should therefore feature much stronger modulations from wave groups. We leave for future work a more thorough investigation of how well KaRIn is able to faithfully capture those local modulations caused by wave groups, but simply point out for the moment that the existence of such a small scale signal makes it very hard to characterize the random noise from the measurement itself (for example by looking at the high frequency variance of the measurement) since the former can often dominate the latter. We also point out that, assuming that the wave group modulations are correctly picked up by KaRIn, this would be a first step towards removing high-frequency noise in KaRIn's topography measurement induced by the local sea state bias variations due to the groups.

Finally, we note that while the agreement between KaRIn and the independent measurements from S3A in the example presented above is one additional piece of evidence illustrating that KaRIn is producing accurate SWH retrievals, a comparison over a large set of such cross-overs would be necessary to provide a more detailed picture of the behavior of KaRIn at a global scale. We leave such a global study for future work.

D. Global comparison against SWOT nadir

One important feature of the comparisons between KaRIN and the other sensors presented in the previous three subsections is that the two measurements being compared were colocated in space, which removes spatial variability of the SWH field as a source of discrepancy obscuring the interpretation of the differences. In this subsection, we present the results of a comparison between KaRIn and SWOT's nadir altimeter. Since both instruments are on the same platform and are operating continuously, this allows for a comparison

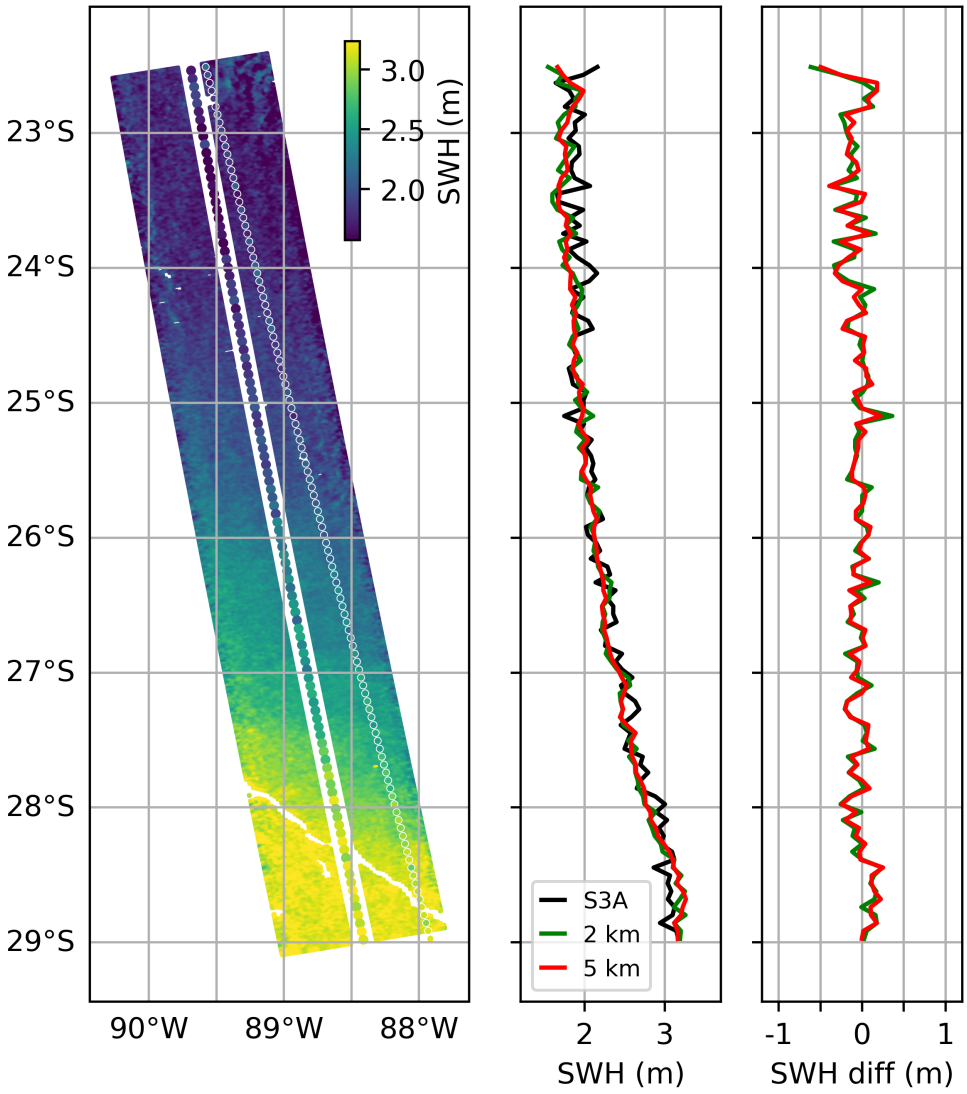

Fig. 8. Example of cross-over between KaRIn (cycle 545, pass 24) and Sentinel 3A (S3A), with about 3h difference in observing times. Left : KaRIn's 2D SWH map, nadir measurements between both swaths and S3A (markers with whtie contours) overlaid on top of KaRIn's swath. Middle : one-dimensional SWH profiles along the S3A track. The north/south gradient is well captured by all instruments. Right : profiles of KaRIn-S3A differences along the S3A track. The bias between both instruments is close to zero.

of simultaneous measurements at the global scale (providing a large sample size to accumulate statistical significance over various observation conditions, such as SWH). The price to pay is of course that both instruments do not measure at the same location, with differences of several tens of kilometers at the edge of KaRIn's swath.

The comparison presented in the subsection was performed over 154 SWOT passes of the 1-day phase : a multidimensional histogram of differences in SWH between KaRIn and the nadir was built as a function of a smooth reference SWH (from the ECMWF model available in the SWOT products) and of cross-track distance. Figure 10 shows probability distribution functions (pdfs) computed from this histogram when integrating over different intervals of cross-track distance (below 20 km, left and above 45 km, right) and of SWH (colors). In what follows, we describe in more details the results of this nadir/KaRIn comparison using percentiles of this type of distribution (possibly integrating over diferent SWH and cross-track distance bins) : Figure 11 reports the median of each distribution while Figure 12 focuses on the width of the distribution defined as half the difference between the 16th and 84th percentile, a quantity we will refer to as the 1σ difference between KaRIn and the nadir. This corresponds to the standard deviation for Gaussian distributions, which is almost exactly the case here.

The median differences of Figure 11, shown for various SWH intervals as a function of cross-track distance can be interpreted as the bias between both instruments under the assumption that on average, the SWH at the nadir track and at any cross-track distance is the same. In other words, we assume that the difference in the true SWH field evaluated at any two different cross-track distances, has a centered distribu-

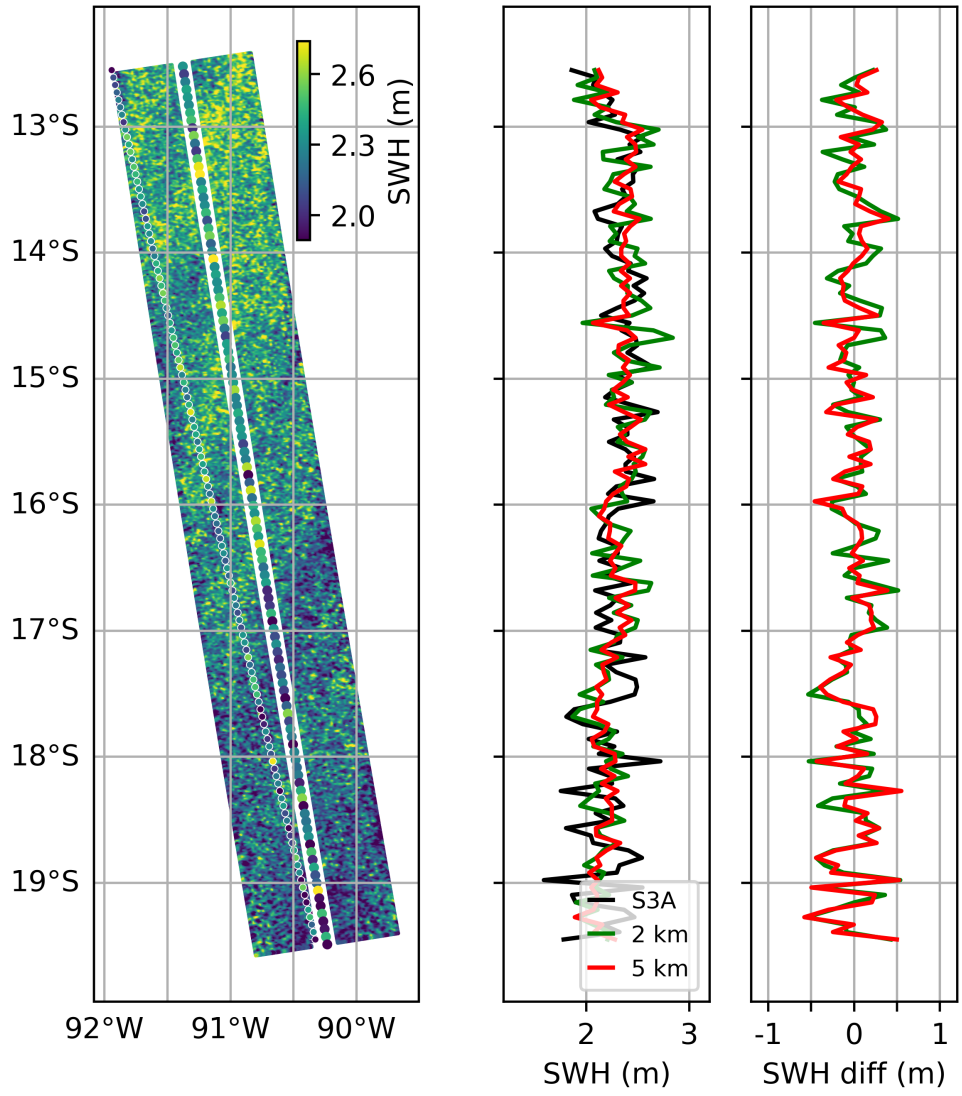

Fig. 9. Second half of the cross-over shown in figure 8, this time as S3A crosses KaRIn's other swath. The high frequency fluctuations in the SWH measurements by all three instruments are much larger than in the previous case, due to the presence of strong modulations from wave groups. This is expected since this case corresponds to a significantly narrower wave spectrum.

tion[4]. For SWH>1 m, those biases are below 5 cm throughout the swath. This increases to about 10 cm for SWH<1 m, which could be expected from the discussion in section II-B since small values of SWH is the most challenging regime. We note that the low SWH regime is also challenging for nadir altimetry, and more validation targeted to this region of parameter space is necessary to understand which instrument is performing better there. This is left for future work. Of course, the resolution at which the SWH is estimated has no impact on the bias, as confirmed by the similarity between the left and right panels.

By contrast, the spatial variability of SWH will of course induce an increase in the variance between the nadir and KaRIn's measurements as the cross-track distance increases. As a result, the 1-sigma SWH difference between nadir and KaRIN shown in Figure12 cannot be easily interpreted in terms of instrumental noise. In fact, the variance in the KaRIn/nadir differences receives contributions from 1) the

[4]Strictly speaking, a sampling bias (completely independent of instrumental effects) can be introduced by this comparison of measurements at different locations, because we are trying to characterize the bias as a function of SWH itself, i.e. we bin the differences in SWH which means that we have to deal with conditional distributions. This should mostly affect the very low and large values of SWH, because they are the least common over the ocean. The origin of this sampling bias can be simply understood by considering the situation where one of the instruments, say instrument A, happens to be measuring over a very low SWH (and therefore very rare) region. More likely than not, the other instrument (B), a few tens of km away from the first, is seeing a larger value of SWH, simply because even lower values are extremely rare. As a result, the differences A-B binned using the values from B will feature a positive bias for very low SWH bins (equivalently, a negative bias would arise if the binning was done with the values from B). In our case, the binning is done in terms of a smooth SWH coming from a model, so we expect such a sampling bias to be attenuated. The exact value of such a bias is difficult to predict as it depends on the spatial correlation of the SWH fields at spatial scales of only a few tens of km, which are not known. In the future, a determination of the purely instrumental bias between KaRIn and nadir altimeters completely free of such a sampling contribution can be achieved from accumulating statistics of differences at cross-overs with other nadir altimeters, similar to the example presented in subsection III-C.

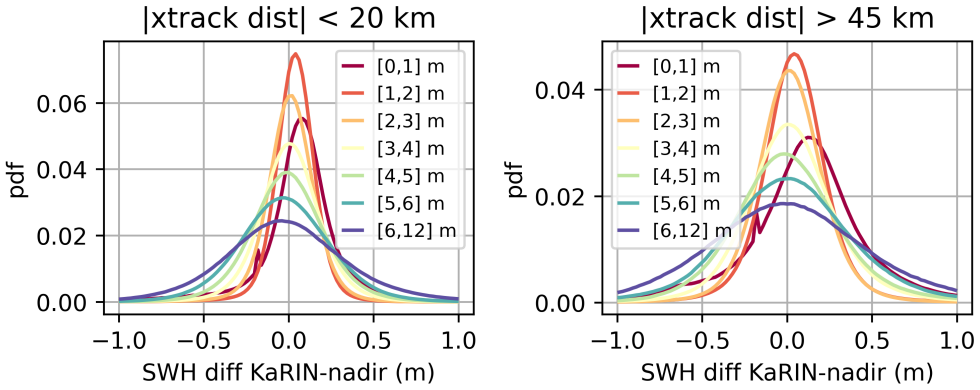

Fig. 10. Probability distribution functions (computed over 154 SWOT passes) of the KaRIn-nadir differences for various SWH bins (colors) and cross-track distance bins (left: near range, right: far range). The center and width of this type of distributions is dicussed in more details in figures 11 and 12, as well as the extent to which they can be interpreted in terms of biases and measurement error.

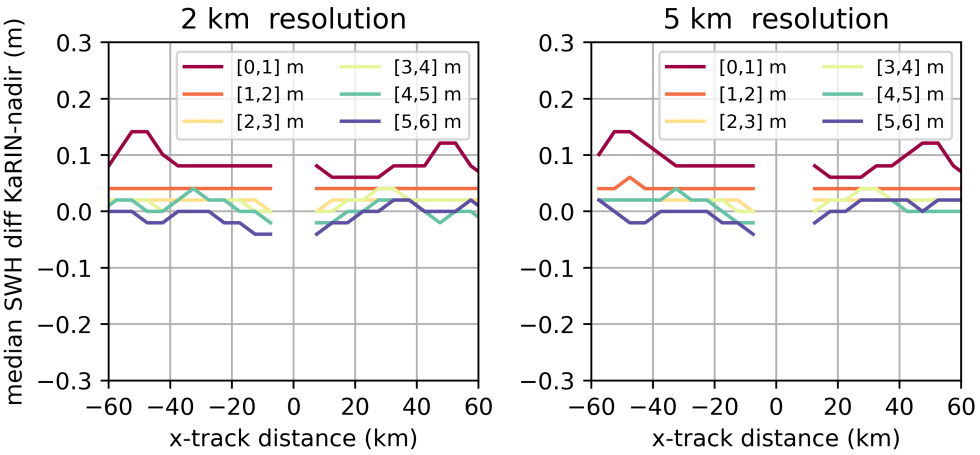

Fig. 11. Median KaRIn-nadir differences as a function of cross-track distance for various SWH bins (colors) and the 2 km (left) and 5 km (right) resolutions. These can be interepreted as relative biases between both instruments, and remain well below 5 cm as soon as SWH>1 m. At lower SWH (the most challenging regime for the inversion), the bias increases to about 10 cm.

geophysical spatial variability in the SWH field, 2) KaRIn's measurement noise and 3) the nadir's measurement noise. The first of these contributions increases with cross-track distance and likely with SWH. We also note that this contribution should increase as the resolution used for the SWH inversion becomes finer since KaRIn then becomes able to pick up additional physical small scale variability such as that generated by the presence of wave groups. The measurement noise in KaRIn can be decomposed into a random contribution and a systematic contribution coming from not having perfectly accounted for all the instrumental sources of decorrelation which vary slowly along the orbit. Both can have an across-track dependance, but only the former should depend on the resolution used for the inversion. According to the discussion in section II-B, we expect the measurement noise in KaRIn to decrease with SWH. Finally, the nadir noise is known to increase with SWH (see for instance [28]) but also depends on other characteristics of the wave spectrum [27].

This mixture of contributions (and the fact that at least the first two depend on SWH, cross-track distance and resolution) makes it difficult to isolate KaRIn's measurement noise from such a KaRIn/nadir contribution. A complementary comparison between KaRIn and the ECMWF wave model will be presented in the next subsection and allows us to characterize the evolution of KaRIn's measurement noise as a function of cross-track distance. Anticipating on the conclusions in there, we point out that the linear trend as a function of cross-track distance visible in Figure 12 is dominated by geophysical variability, while the sharp increase visible for lower values of SWH towards the edges of the swath can be attributed to (systematic) measurement noise in KaRIn. The non-trivial ordering of the 1σ differences as a function of SWH (say at 10 km cross-track distance) which start by decreasing with SWH (until $\approx$ 2 m) before increasing towards large values of SWH results from competing effects : both the nadir noise and the geophysical variability increase with SWH, while the KaRIn noise decreases.

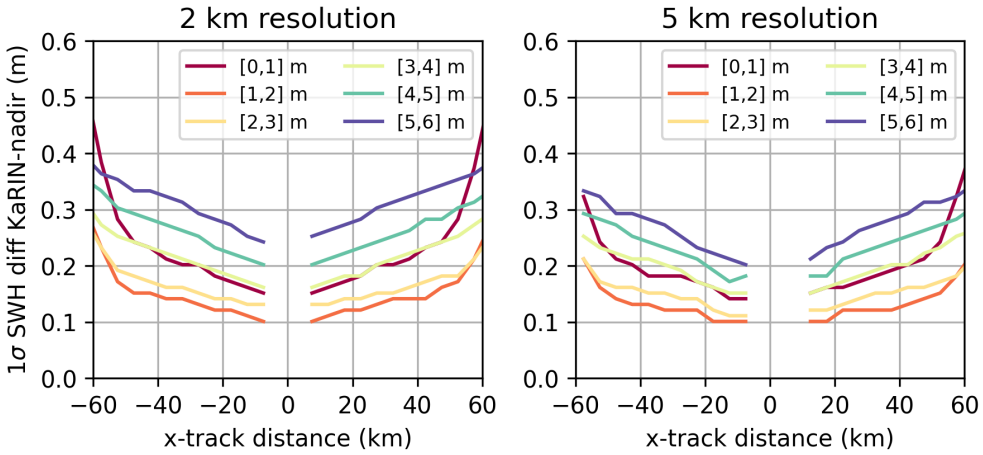

Fig. 12. 1σ difference (i.e. half the difference between the 84th and 16th percentiles of the distribution) between KaRIn and nadir. This receives contributions from the measurement error in both the nadir instrument and in KaRIn, as well as from spatial variability between the measurement locations of both instruments. The linear trend as a function of cross-track distance is dominated by this geophysical spatial variability, while the sharper increase towards the outer edge of the swaths, particularly visible for low SWH, is attributable to increased measurement error in KaRIn, as discussed in section III-E.

E. Global comparison against the ECMWF wave model

In this subsection, we reproduce the previous comparison but replacing SWOT's nadir measurements by the SWH computed by the ECMWF model [29], which is conveniently provided in the SWOT products. The main advantage with respect to the KaRIn/nadir comparison is that differences can be computed at the same location, which will get us rid of the increase in variance with cross-track distance due to spatial variability in the SWH field. However, spatial variability will of course remain a limiting factor in this comparison given the lack of current forcing in the model : small scale gradients are typically missed by the model. As an illustration that the lack of small scales will usually dominate the differences between KaRIn and the model, figure 13 shows the SWH field measured by KaRIn at 2 km resolution (left; same as the left panel of figure 4, reproduced here for the reader's convenience) and predicted by the model (right) for the case already shown in section II-D and which features strong SWH gradients (also seen by the nadir instrument) due to wave-current interactions. Since the model does not account for current effects on waves, it fails to capture the current induced gradients in the SWH field, such as the narrow region of high SWH oriented in the SW-SE direction (note that the colorbars are different; using the same for both plots would have resulted in an almost uniform right panel).

The case presented in figure 13 is far from being an extreme event and the KaRIn/model differences will often be completely dominated by the lack of small scales in the model. Despite that, this comparison is useful in understanding some of the properties of KaRIn's measurement error because the contribution to the variance of the KaRIn/model differences from this small scale SWH variability not captured by the model should not depend on cross-track distance. In fact, the only two contributions to this variance should now be 1) the error in the model (both small scales which are missed and possible errors on the larger scales) and 2) KaRIn's measurement noise.

The 1σ KaRIn/model differences for various SWH bins are shown in figure 14 as a function of cross-track distance. Once again, we ephasize that the differences are usually dominated by the missing content in the model, so the values shown in the plot are at best loose upper bounds of the KaRIn measurement noise[5]. However, all the cross-track dependence in that plot can be now interpreted as an increase in measurement noise.

To quantify this further, figure 15 shows the increase in variance at any cross-track distance with respect to the near range (average of the first few of each swath). As expected, the measurement noise increases more steeply for low SWH values and towards the outer edge of the swath. For SWH$>$1 m, the additional variance with respect to the near range remains below $0.05\,m^2$ ($0.1\,m^2$ below 1 m) up to 50 km in across-track confirming that the linear trend of several tens of cm visible in the cross-track profiles of the KaRIn/nadir comparison of figure 12 were due to geophysical variability. Above 50 km, KaRIn's measurement noise increases more significantly and exceeds several tens of centimers in the last km of the swath (assuming that the noise in the far range is much larger than the noise in the near range, the additional variance shown in this plot can be interpreted as total variance).

Since the curves at 2 km (solid) and 5 km (dashed) resolution are close to each other, this excess measurement noise towards the edge of the swath is mostly not random, but

[5]We note that the reduction in variance between the 2 km and the 5 km resolutions is a combination of reduced measurement noise and smoothing of group modulations at scales below 5 km. In other words, comparing the 2 km and 5 km 1σ errors does not allow to quantify the random component of the measurement noise. This is confirmed by reproducing the figure (not shown) but separating each SWH bin into cases with pure wind seas (where no strong group modulations are expected) and cases with strong swells (which typically have peakier spectra giving rise to stronger group modulations). The 1σ differences are consistently larger for the cases with swells, consistent with the fact that the modulation from groups is an important contributor to the KaRIn/model differences.

This article has been accepted for publication in IEEE Transactions on Geoscience and Remote Sensing. This is the author's version which has not been fully edited and content may change prior to final publication. Citation information: DOI 10.1109/TGRS.2025.3551605

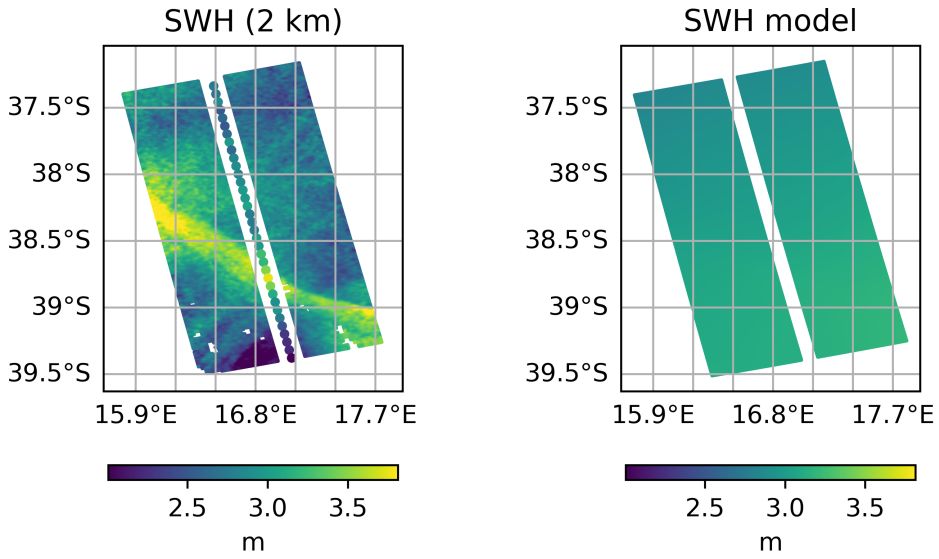

Fig. 13. Same as figure 4 but with the right panel showing the ECMWF SWH instead of the KaRIn measurements at 5 km resolution. The model is very smooth and misses the physical features seen in the left panel. This dominates the variance of the KaRIn-model differences, which as a result cannot be interpreted in terms of absolute levels of measurement noise. As argued in the rest of this subsection, this KaRIn vs model comparison does still provide some characteriztion of KaRIn's error, since relative variations with cross-track distance of the variance of the differences is necessarily attributable to measurement error.

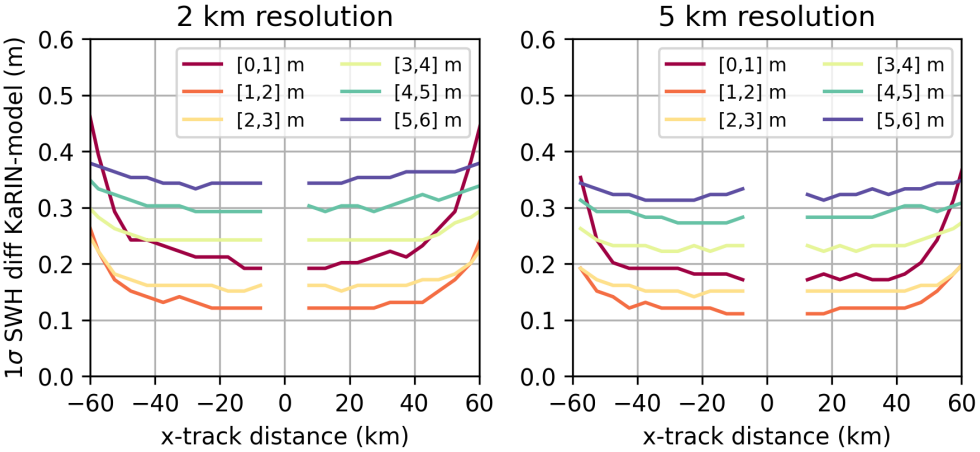

Fig. 14. Same as figure 12 but with the nadir replaced by the model. The linear increase with cross-track distance of figure 12, due to the geophysical spatial variability between the measurement locations of the nadir and KaRIn has disappeared. However, the 1σ differences are mostly dominated by the high frequency signal misssing in the model and are not representative of KaRIn measurement error. However, this missing signal in the model has no reason to depend on cross-track distance. All the variations with cross-track distance, in particular the steep increase seen in the outer edges of the swaths at low SWH, come from measurement error increasing with cross-track distance.

rather comes from an imperfect modeling of the systematic sources of instrumental decorrelation which vary in along track. For low SWH values in particular, our 10^{-4} accuracy on those instrumental effects becomes insufficient. Given that these instrumental decorrelation errors tend to vary slowly in along-track, the additional measurement error evidenced in this section will usually manifest itself as a slowly evolving bias at the edge of the swath over scences of a few hundred of kilometers. One example of this can be seen in the top left corner of Figure 6. This also explains the negative bias seen against MASS for the larger cross-track distances (bottom right histogram in figure 7). If the MASS flights had taken place at a different latitude, this local bias would likely have been different.

IV. Discussion

Having described the method used to estimate SWH from KaRIn measurements and having validated those estimates against those obtained with independent methods (allowing us to at least partially characterize the measurement noise), we conclude this article by discussing some applications and avenues for research that this new dataset opens.

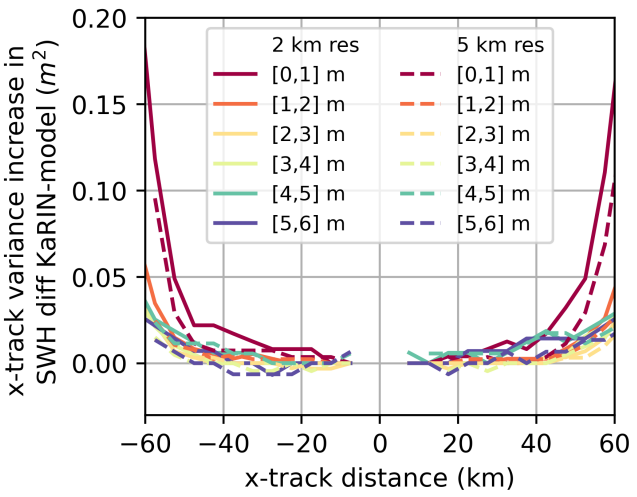

Fig. 15. Variance increase (with respect to near range) of the KaRIn-model differences. This is entirely attributable to KaRIn's measurement error. As could be expected from the discussion in section II-B, this is larger in the far range and for low SWH values.

By providing for the first time at the global scale two-dimensional maps of SWH at a resolution of a few kilometers, the SWOT mission creates an opportunity to better understand at much finer scale than before the physical phenomena that shape the sea state variability, such as wave-current interactions [17]–[21] and wind forcing [30]–[32]. Indeed, part of what makes KaRIn a unique instrument for the study of waves is that, in addition to providing SWH maps, it provides simultaneous maps of σ_0 and of surface topography, from which geostrophic velocities can be computed (below, we use those provided in [33]) and used as a proxy for currents.

Figures 16 and 17 illustrate geostrophic velocity, SWH, and σ_0 in two distinct geographical regions. Both figures reveal a striking similarity in the spatial structure of all three fields. Notably, strong gradients in SWH are observed near current gradients, generally coinciding with modulations of σ_0, suggesting a strong coupling between currents, waves, and winds.

In Figure 16 (Agulhas current; same example as in Figure 4), the observed spatial variability of SWH is consistent with swell from the Southern Ocean interacting with strong mesoscale currents and meanders [34], [35]. Figure 17, shows an example located in the Gulf Stream region. Wave spectrum from a hindcast (not shown) indicates that the wave field during that time was dominated by locally generated waves with relatively low SWH. Despite the differences in sea state compared to the Agulhas Current case, Figure 17 still demonstrates similar correspondences between currents, SWH, and σ_0 features.

Currents are the largest source of spatial variability of SWH at scales under 100 km [17], [20], [27], and most of this effect can be attributed to refraction [18], [35]–[37]. However, it is important to note that the effects of refraction are both local and non-local, meaning current gradients can lead to SWH gradients far downstream from the current patterns [37]–[39]. Current effects on waves can also lead to modulations of the sea surface roughness, which would show up as modulations of σ_0. Therefore, σ_0 can be sensitive to wave-current interactions in addition to wind speed (e.g. [40]). We note that other phenomena such as the presence of surfactants or surface heat fluxes also impact the σ_0 and can make the interpretation of these joint current/SWH/σ_0 complex in certain situations. Figures 16 and 17 highlight the intricate coupling between currents, waves, and winds and showcase the potential of SWOT observations to shed light on these complex interactions. Diagnosing the underlying mechanisms driving the observed gradients in SWH and σ_0 is beyond the scope of this work and will be explored in a separate manuscript.

V. Summary

We have demonstrated that the interferometric data from KaRIn can be processed into spatial maps of SWH. The measured (total) interferometric correlation is first processed into volumetric decorrelation by factoring out all instrumental contributions. Due to the high accuracy that is needed, this required a combination of instrumental modelling and a simple and static empirical calibration designed to correct for unmodelled sources of instrumental decorrelation and for inaccuracies in modelling the known ones. The calibrated volumetric decorrelation, originally available at KaRIn's native 500 m resolution (in LR mode), is then converted into SWH after some local averaging to 2 km or 5 km. We have validated KaRIn's SWH retrievals against independent data, namely from a GPS buoy, from MASS's airborne lidar, from Sentinel3's SAR altimeter, from SWOT's nadir altimeter and from a numerical wave model. We have shown in figures 5, 6, 7, 8, 9 and 11 that relative biases between KaRIn and all these datasets are of the order of centimeters. We expect that such spatial maps of SWH will contribute to a better understanding of the sources of SWH spatial variability at small scales.

Aknowledgements

Part of this work was funded by the French Space agency (CNES) in the context of the SWOT development program. A portion of this work was carried out at the Jet Propulsion Laboratory, California Institute of Technology, under a contract with the National Aeronautics and Space Administration (80NM0018D0004). L. Lenain was funded by JPL1674228 contract. A. Hay is supported by a Research Training Program scholarship from the Australian government and a Postgraduate Studentship from CSIRO. SOTS data were sourced from Australia's Integrated Marine Observing System (IMOS) - IMOS is enabled by the National Collaborative Research Infrastructure Strategy (NCRIS). A. B. Villas Bôas was supported by NASA awards 80NSSC23K0979 through the IOVW science team and 80NSSC24K1640 through the SWOT science team.

References

[1] L. Fu, T. Pavelsky, J. Cretaux, R. Morrow, J. T. Farrar, P. Vaze, P. Sengenes, N. Vinogradova-Shiffer, A. Sylvestre-Baron, N. Picot, and G. Dibarboure, "The surface water and ocean topography mission: A breakthrough in radar remote sensing of the ocean and land surface water," *Geophysical Research Letters*, vol. 51, no. 4, Feb. 2024.

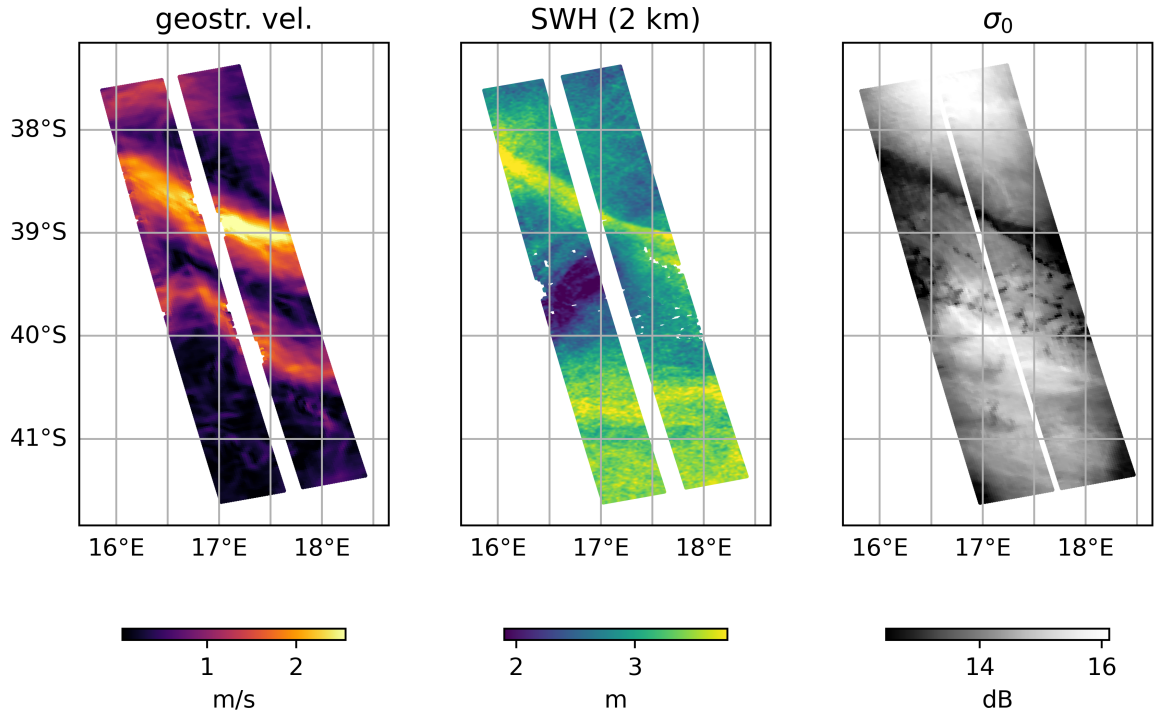

Fig. 16. Example of geostrophic velocities (left), SWH (middle) and σ_0 (right) measured by KaRIn during cycle 481 and pass 16 over the Agulhas current. Strong correlations between all three fields are clearly visible. The combined observation by KaRIn of these three quantities should help advance our understanding of the phenomena that drive the small scale structures of the SWH field, particularly wave-current interactions and wind forcing.

[2] E. Peral and D. Esteban-Fernandez, "SWOT mission performance and error budget." Valencia, Spain: IEEE, 2018, pp. 8625–8628.

[3] E. Peral, D. Esteban-Fernandez, E. Rodríguez, D. McWatters, J. D. Bleser, R. Ahmed, A. C. Chen, E. M. Slimko, R. Somawardhana, K. Knarr, M. Johnson, S. Jaruwatanadilok, S. F. Chan, X. Wu, D. Clark, K. Peters, C. W. Chen, P. Mao, B. Khayatian, J. Chen, R. E. Hodges, D. Boussalis, B. W. Stiles, and K. Srinivasan, "KaRIn, the Ka-Band radar interferometer of the SWOT mission: Design and in-flight performance," *IEEE Trans. Geosci. Remote. Sens.*, vol. 62, pp. 1–27, 2024.

[4] R. Morrow, L.-L. Fu, F. Ardhuin, M. Benkiran, B. Chapron, E. Cosme, F. d'Ovidio, J. T. Farrar, S. T. Gille, G. Lapeyre, P.-Y. Le Traon, A. Pascual, A. Ponte, B. Qiu, N. Rascle, C. Ubelmann, J. Wang, and E. D. Zaron, "Global observations of fine-scale ocean surface topography with the surface water and ocean topography (SWOT) mission," *Frontiers in Marine Science*, vol. 6, May 2019.

[5] E. Rodriguez and J. Martin, "Theory and design of interferometric synthetic aperture radars," *IEE Proceedings F Radar and Signal Processing*, vol. 139, no. 2, p. 147, 1992.

[6] P. Rosen, S. Hensley, I. Joughin, F. Li, S. Madsen, E. Rodriguez, and R. Goldstein, "Synthetic aperture radar interferometry," *Proceedings of the IEEE*, vol. 88, no. 3, pp. 333–382, Mar. 2000.

[7] D. Stammer, *Satellite altimetry over oceans and land surfaces*, ser. Earth observation of global changes, A. Cazenave, Ed. Boca Raton: CRC Press, 2018.

[8] JPL, "D-61923, Revision B. KaRIn: Ka-band Radar Interferometer On-Board Processor (OBP) Algorithm Theoretical Basis Document (ATBD), Jet Propulsion Laboratory Internal Document," 2021. [Online]. Available: http://archive.podaac.earthdata.nasa.gov/podaac-ops-cumulus-docs/web-misc/swot_mission_docs/D-79130_KaRIn_OBP_ATBD_RevBwesign.pdf

[9] ——, "D-105501, Revision B. SWOT Algorithm Theoretical Basis Document: KaRIn Level 1B Low Rate Interferogram (L1B-LR-INTF) Science Algorithm Software, Jet Propulsion Laboratory Internal Document." 2023. [Online]. Available: https://archive.podaac.earthdata.nasa.gov/podaac-ops-cumulus-docs/web-misc/swot_mission_docs/atbd/D-105501_SWOT_ATBD_L1B_LR_INTF_20230724_cite.pdf

[10] ——, "D-105502, Revision B. SWOT Algorithm Theoretical Basis Document: KaRIn Level 2 Low Rate Sea Surface Height (L2-LR-SSH) Science Algorithm Software, Jet Propulsion Laboratory Internal Document." 2023. [Online]. Available: https://archive.podaac.earthdata.nasa.gov/podaac-ops-cumulus-docs/web-misc/swot_mission_docs/atbd/D-105502_SWOT_ATBD_L2_LR_SSH_20230724a_cite.pdf

[11] C. W. Chen, "A spectral model for multilook insar phase noise due to geometric decorrelation," *IEEE Transactions on Geoscience and Remote Sensing*, vol. 61, pp. 1–11, 2023.

[12] A. Bohé, "A complete theoretical derivation of the level of random height noise in interferometric unfocused sar swath altimetry," *IEEE Transactions on Geoscience and Remote Sensing*, vol. 61, pp. 1–29, 2023.

[13] E. Peral, E. Rodríguez, and D. Esteban-Fernández, "Impact of surface waves on SWOT's projected ocean accuracy," *Remote Sensing*, vol. 7, no. 11, pp. 14 509–14 529, Nov. 2015.

[14] JPL, "D-109532, Initial Release. SWOT Science Data Products User Handbook, Jet Propulsion Laboratory Internal Document." 2024. [Online]. Available: https://archive.podaac.earthdata.nasa.gov/podaac-ops-cumulus-docs/web-misc/swot_mission_docs/D-109532_SWOT_UserHandbook_20240502.pdf

[15] R. Touzi and A. Lopes, "Statistics of the stokes parameters and of the complex coherence parameters in one-look and multilook speckle fields," *IEEE Transactions on Geoscience and Remote Sensing*, vol. 34, pp. 519–531, 1996.

[16] R. Touzi, A. Lopes, J. Bruniquel, and P. Vachon, "Coherence estimation for sar imagery," *IEEE Transactions on Geoscience and Remote Sensing*, vol. 37, pp. 135–149, Jan. 1999.

[17] F. Ardhuin, S. T. Gille, D. Menemenlis, C. B. Rocha, N. Rascle, B. Chapron, J. Gula, and J. Molemaker, "Small-scale open ocean currents have large effects on wind wave heights," *Journal of Geophysical Research: Oceans*, vol. 122, no. 6, pp. 4500–4517, Jun. 2017.

[18] A. B. Villas Bôas, B. D. Cornuelle, M. R. Mazloff, S. T. Gille, and F. Ardhuin, "Wave–current interactions at meso- and submesoscales: Insights from idealized numerical simulations," *Journal of Physical Oceanography*, vol. 50, no. 12, pp. 3483–3500, Dec. 2020.

[19] L. Romero, D. Hypolite, and J. C. McWilliams, "Submesoscale current effects on surface waves," *Ocean Modelling*, vol. 153, p. 101662, Sep.

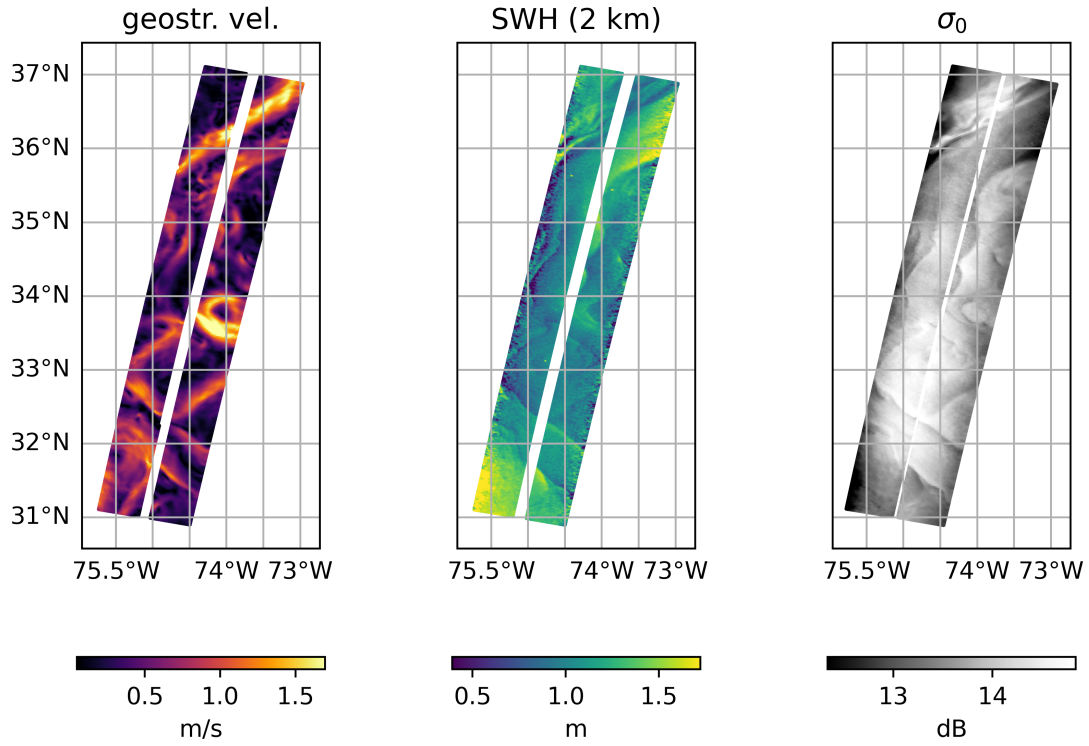

Fig. 17. Same as figure 16 but for cycle 490 and pass 9, over the Gulf Stream. Here again, strong correlations between the currents, the waves and the σ_0 are clearly visible. In this example, some correlated structures appear in the SWH and σ_0 without any corresponding signature in the currents, potentially suggesting that local wind forcing plays a role in shaping the SWH field at least in this low SWH case.

2020.

[20] Y. Quilfen and B. Chapron, "Ocean surface wave-current signatures from satellite altimeter measurements," *Geophysical Research Letters*, vol. 46, no. 1, pp. 253–261, Jan. 2019.

[21] L. Lenain, B. K. Smeltzer, N. Pizzo, M. Freilich, L. Colosi, S. A. Ellingsen, L. Grare, H. Peyriere, and N. Statom, "Airborne remote sensing of upper-ocean and surface properties, currents and their gradients from meso to submesoscales," *Geophysical Research Letters*, vol. 50, no. 8, Apr. 2023.

[22] M. De Carlo and F. Ardhuin, "Along-track resolution and uncertainty of altimeter-derived wave height and sea level: Re-defining the significant wave height in extreme storms," *Journal of Geophysical Research: Oceans*, vol. 129, no. 6, Jun. 2024.

[23] W. Bertiger, Y. Bar-Sever, A. Dorsey, B. Haines, N. Harvey, D. Hemberger, M. Heflin, W. Lu, M. Miller, A. W. Moore, D. Murphy, P. Ries, L. Romans, A. Sibois, A. Sibthorpe, B. Szilagyi, M. Vallisneri, and P. Willis, "Gipsyx/rtgx, a new tool set for space geodetic operations and research," *Advances in Space Research*, vol. 66, no. 3, pp. 469–489, Aug. 2020.

[24] A. Hay, C. Watson, B. Legresy, M. King, and J. Beardsley, "In situ validation of altimetry and CFOSAT SWIM measurements in a high wave environment," *Journal of Atmospheric and Oceanic Technology*, vol. 40, no. 10, pp. 1137–1152, Oct. 2023.

[25] W. K. Melville, L. Lenain, D. R. Cayan, M. Kahru, J. P. Kleissl, P. F. Linden, and N. M. Statom, "The modular aerial sensing system," *Journal of Atmospheric and Oceanic Technology*, vol. 33, no. 6, pp. 1169–1184, Jun. 2016.

[26] L. Lenain and W. K. Melville, "Measurements of the directional spectrum across the equilibrium saturation ranges of wind-generated surface waves," *Journal of Physical Oceanography*, vol. 47, no. 8, pp. 2123–2138, Aug. 2017.

[27] M. De Carlo, F. Ardhuin, A. Ollivier, and A. Nigou, "Wave groups and small scale variability of wave heights observed by altimeters," *Journal of Geophysical Research: Oceans*, vol. 128, no. 8, Jul. 2023.

[28] C. Tourain, F. Piras, A. Ollivier, D. Hauser, J. C. Poisson, F. Boy, P. Thibaut, L. Hermozo, and C. Tison, "Benefits of the adaptive algorithm for retracking altimeter nadir echoes: Results from simulations and CFOSAT/SWIM observations," *IEEE Transactions on Geoscience and Remote Sensing*, vol. 59, pp. 9927–9940, Dec. 2021.

[29] P. A. Janssen and J.-R. Bidlot, "Progress in operational wave forecasting," *Procedia IUTAM*, vol. 26, pp. 14–29, 2018.

[30] S. Abdalla and L. Cavaleri, "Effect of wind variability and variable air density on wave modeling," *Journal of Geophysical Research: Oceans*, vol. 107, no. C7, Jul. 2002.

[31] H. L. Tolman, "Treatment of unresolved islands and ice in wind wave models," *Ocean Modelling*, vol. 5, no. 3, pp. 219–231, Jan. 2003.

[32] F. Ardhuin, E. Stutzmann, M. Schimmel, and A. Mangeney, "Ocean wave sources of seismic noise," *Journal of Geophysical Research*, vol. 116, no. C9, Sep. 2011.

[33] DESMOS Science team project, "SWOT Level-3 SSH Expert (Version 1.0). The SWOT L3 SSH product is derived from the L2 SWOT KaRIn Low rate ocean data products from NASA/JPL and CNES," 2023. [Online]. Available: https://www.aviso.altimetry.fr/en/data/products/sea-surface-height-products/global/swot-l3-ocean-products.html

[34] Y. Quilfen, M. Yurovskaya, B. Chapron, and F. Ardhuin, "Storm waves focusing and steepening in the agulhas current: Satellite observations and modeling," *Remote Sensing of Environment*, vol. 216, pp. 561–571, Oct. 2018.

[35] G. Marechal and F. Ardhuin, "Surface currents and significant wave height gradients: Matching numerical models and high-resolution altimeter wave heights in the agulhas current region," *Journal of Geophysical Research: Oceans*, vol. 126, no. 2, Feb. 2021.

[36] A. B. V. Bôas and W. R. Young, "Directional diffusion of surface gravity wave action by ocean macroturbulence," *Journal of Fluid Mechanics*, vol. 890, p. R3, 2020.

[37] H. Wang, A. B. Villas Bôas, W. R. Young, and J. Vanneste, "Scattering of swell by currents," *Journal of Fluid Mechanics*, vol. 975, p. A1, 2023.

[38] F. Ardhuin, A. Roland, F. Dumas, A.-C. Bennis, A. Sentchev, P. Forget, J. Wolf, F. Girard, P. Osuna, and M. Benoit, "Numerical wave modeling in conditions with strong currents: Dissipation, refraction, and relative wind," *Journal of Physical Oceanography*, vol. 42, no. 12, pp. 2101–2120, 2012.

[39] B. S. White and B. Fornberg, "On the chance of freak waves at sea," *Journal of Fluid Mechanics*, vol. 355, pp. 113 – 138, 1998. [Online]. Available: https://api.semanticscholar.org/CorpusID:1299374

[40] N. Rascle, F. Nouguier, B. Chapron, A. Mouche, and A. Ponte, "Surface roughness changes by finescale current gradients: Properties at multiple azimuth view angles," *Journal of Physical Oceanography*, vol. 46, no. 12, pp. 3681 – 3694, 2016. [Online]. Available: https://journals.ametsoc.org/view/journals/phoc/46/12/jpo-d-15-0141.1.xml